Glutaminase as a metabolic target of choice to counter acquired resistance to Palbociclib by colorectal cancer cells

Míriam Tarrado-Castellarnau[1,2,*], Carles Foguet[1,2,3,*], Josep Tarragó-Celada[1,4], Marc Palobart[1], Claudia Hernández-Carro[1,2], Jordi Perarnau[1], Erika Zodda[1,8], Ibrahim H. Polat[1,2], Silvia Marin[1,2], Alejandro Suarez-Bonnet[5,6], Juan José Lozano[7], Mariia Yuneva[4], Timothy M. Thomson[2,8,9 †], Marta Cascante[1,2, †]

[1] Department of Biochemistry and Molecular Biomedicine and Institute of Biomedicine (IBUB), Universitat de Barcelona, Barcelona, Spain.

[2] CIBER of Hepatic and Digestive Diseases (CIBEREHD), Institute of Health Carlos III (ISCIII), Madrid, Spain.

[3] British Heart Foundation Cardiovascular Epidemiology Unit and Victor Phillip Dahdaleh Heart and Lung Research Institute, University of Cambridge, Cambridge, UK.

[4] Oncogenes and Tumour Metabolism Laboratory, The Francis Crick Institute, London, UK.

[5] Experimental Histopathology, The Francis Crick Institute, London, UK.

[6] Department of Pathobiology and Population Sciences, The Royal Veterinary College, Hatfield, UK.

[7] Bioinformatics Platform, Centro de Investigación Biomédica en Red Enfermedades Hepáticas y Digestivas (CIBEREHD), Barcelona, Spain.

[8] Institute for Molecular Biology (IBMB-CSIC), Barcelona, Spain.

[9] Instituto de Investigaciones de la Altura, Universidad Peruana Cayetano Heredia, Lima, Peru

* Equal contribution

[†] Corresponding authors: Timothy M Thomson, Barcelona Institute for Molecular Biology (IBMB-CSIC), Barcelona, e-mail titbmc@ibmb.csic.es; Marta Cascante, Universitat de Barcelona, Barcelona, e-mail martacascante@ub.edu

Summary

Therapeutic resistance in cancer emerges from genetic or epigenetic mechanisms that enable cell survival under drug pressure. While several resistance mechanisms to cyclin-dependent kinase inhibitors have been identified, acquired resistance is still a therapeutic challenge. Here, we have systematically analyzed metabolic reprogramming in colorectal cancer cells exposed to Palbociclib, a CDK4/6 inhibitor, or Telaglenestat, a glutaminase inhibitor. Through multiple approaches, we show that Palbociclib and Telaglenestat elicit complementary metabolic responses and are thus uniquely suited to counter the metabolic reprogramming induced by the reciprocal drug. As such, while Palbociclib induced reduced tumor growth *in vivo*, and Telaglenestat did not show a significant effect, the drug combination displayed a strong synergistic effect on tumor growth. Likewise, initial responses to Palbociclib were followed by signs of adaptation and resistance, which were prevented by combining Palbociclib with Telaglenestat. Our findings reveal that Palbociclib and Telaglenestat combination can effectively forestall acquired resistance to Palbociclib.

Introduction

Cell cycle control is frequently dysregulated in cancer cells leading to unscheduled proliferation (Diaz-Moralli et al., 2013). Cyclin-dependent kinases CDK4 and CDK6 (CDK4/6) are promising targets in cancer therapy since their overexpression is implicated in a wide range of human cancers (Goel et al., 2022; Sherr et al., 2016). Three selective pharmacologic CDK4/6 inhibitors have received approval from the US Food and Drug Administration (FDA) and the European Medicines Agency (EMA) for the treatment of hormone receptor (HR)-positive, human epidermal growth factor receptor 2 (HER2)-negative locally advanced or metastatic breast cancer (Groenland et al., 2020). Among these, Palbociclib (PD0332991) was the first-in-class drug to show promising results in phase III studies (Beaver et al., 2015; Marra and Curigliano, 2019; O'Leary et al., 2016). However, like with most targeted therapies, tumor cells eventually acquire resistance to CDK4/6 inhibition (McCartney et al., 2019). In this regard, tumor metabolic reprogramming plays a crucial role in the adaptive response to chemotherapy, and its analysis can unveil *de novo* vulnerabilities that can be targeted to overcome drug-resistant states (Desbats et al., 2020; Tarrado-Castellarnau et al., 2016).

Our previous work accurately described the metabolic reprogramming associated with CDK4/6 inhibition or depletion, uncovering the upregulation of MYC, glutaminolysis, and mTOR signaling as a consequence of and major adaptation of colorectal cancer cells (Tarrado-Castellarnau et al., 2017). Our results demonstrated that these MYC-driven adaptations to CDK4/6 inhibition render cancer cells highly sensitive to MYC, glutaminase, or mTOR inhibitors and hypoxic conditions. As such, we validated the combined inhibition of CDK4/6 and glutaminase (GLS1) as an effective strategy to forestall resistance to CDK4/6 therapy with strong synergistic and selective antiproliferative effects on tumor cells *in vitro*.

Herein, we have analyzed the metabolic reprogramming associated with the inhibition of CDK4/6 or GLS1, and their combination, both *in vitro* and *in vivo*, in a mouse

xenograft model of HCT116 human colorectal cancer cells. Using genome-scale metabolic modeling, we have integrated transcriptomics and metabolomics data to systematically reveal the most relevant up- and down-regulated metabolic pathways in colorectal cancer cells in response to single or combined *in vivo* therapies, confirming that the combined treatment with Palbociclib and Telaglenestat (CB-839, a selective GLS1 inhibitor) counteracts the adaptive response of tumor cells to Palbociclib as a single therapeutic agent, thus averting the acquisition of pharmacological resistance. Remarkably, we have found that residual cancer cells from tumors treated *in vivo* with the combined therapy remain sensitive to the dual treatment *ex vivo*, long after chemotherapeutic exposure, and exhibit a downregulated metabolism. Together, our results validate the combination of Palbociclib and Telaglenestat as an effective strategy to prevent pharmacologic resistance and improve the antiproliferative effects of the single-agent treatment.

Results

Metabolic adaptations of HCT116 cells to prolonged treatment with Palbociclib and Telaglenestat

Our previous investigations revealed that the combined therapy with CDK4/6 and glutaminase inhibitors presented strong antiproliferative synergies in colon cancer cells with no significant cytotoxic effects on non-malignant cells (Tarrado-Castellarnau et al., 2017), predicting for this combination a promising therapeutic use in cancer treatment. As such, we first characterized *in vitro* the antiproliferative effects of Telaglenestat (CB-839) (Supplementary Figure 1A), alone and in combination with Palbociclib (PD0332991), since it is a selective glutaminase inhibitor of both splice variants of glutaminase (KGA and GAC) with good oral bioavailability (Gross et al., 2014; Harding et al., 2021) and is currently in phase II clinical trials (NCT04265534). In contrast, the classical glutaminase inhibitor, BPTES, has poor metabolic stability and low solubility,

limiting its potential for *in vivo* assays and requiring further clinical development (Shukla et al., 2012). The combination of Palbociclib and Telaglenestat presented strong synergistic antiproliferative effects over a wide dose range (CI < 0.3) (Figure 1A and Supplementary Figure 1B) on HCT116 colorectal cancer cells, as well as a reduction in anchorage-independent growth (Figure 1B) and clonogenic potential (Figure 1C). We also observed a synergistic effect on cell cycle arrest at the G1 phase in the combined condition (Figure 1D). Unexpectedly, while Palbociclib imposed a pronounced antiproliferative effect on HCT116 cells (Figure 1E,F and Supplementary Figure 1C), the cell doubling time was only marginally increased (Figure 1G), suggesting an early inhibition of cell division with a subsequent adaptation to this drug. Glutaminase inhibition alone had no impact on cell proliferation or duplication time. In contrast, the combined treatment caused a significant rise in cell doubling time compared to all groups and, consequently, a greater inhibitory effect on cell proliferation (Figure 1E-G and Supplementary Figure 1C). Collectively, these results corroborate that glutaminase inhibition synergizes with Palbociclib to impair HCT116 colon cancer cell proliferation *in vitro*.

To determine whether the cellular response triggered by the inhibitors was exposure-time dependent, we treated HCT116 cells with Palbociclib, Telaglenestat, and their combination for 24, 48, 96, and 192 h. By analyzing the protein levels of central metabolism regulators, we observed that Palbociclib caused an activation of the mTOR, MYC, and AKT signaling pathways, which reached peak levels at 96 h of treatment (Figure 1H). On the other hand, Telaglenestat induced an earlier activation of these pathways, as well as an upregulation of HIF-1α, while glutaminase protein levels were only increased at 192 h of treatment. Remarkably, the levels of MYC and P-AKT substantially decreased at 192 h in all cases, revealing a metabolic reprogramming dependent on the drug exposure time. We also observed that the drug combination prevented MYC early activation compared to either treatment alone.

Next, we assessed the cellular consumption and production rates of the major carbon sources at 96 and 192 h of treatment. In line with our previous results (Tarrado-Castellarnau et al., 2017), cells subjected to a 96 h incubation with Palbociclib displayed enhanced rates of glucose and glutamine consumption and of lactate and glutamate production (Figure 1I), which is also in agreement with the reported activation of mTOR, MYC, and AKT signaling pathways and increased protein levels of glutaminase (Figure 1H). However, after 192 h of treatment, the metabolic reprogramming of Palbociclib-treated cells shifted to a reduced glycolytic profile while remaining highly glutaminolytic (Figure 1J). On the other hand, Telaglenestat partially inhibited glutaminolysis and increased glucose consumption and lactate production, both at 96 and 192 h. Interestingly, the metabolic adaptation triggered by the combined treatment displayed the greatest increase in glucose uptake and lactate release at both incubation times. The combination of inhibitors also prompted an increment in the glutaminolytic flux at 96 h compared to control and Telaglenestat-treated conditions, significantly increasing after eight days of treatment and in accordance with the upregulation of GLS1 protein levels reported at 192 h (Figure 1H).

Palbociclib and Telaglenestat combined therapy presents synergistic antiproliferative effects *in vivo*

To validate our *in vitro* results, we investigated the effects of the combined administration of Palbociclib and Telaglenestat on the tumor growth of HCT116 cells xenografted into non-obese diabetic (NOD) severe combined immunodeficiency disease (SCID) mice. One week after HCT116 subcutaneous injection, mice were treated with either vehicle (Control), Palbociclib (100 mg/kg/day p.o.), Telaglenestat (150 mg/kg/day p.o.), or Palbociclib + Telaglenestat (100 mg/kg/day p.o. + 150 mg/kg/day p.o.) for 23 days (Supplementary Figure 2A). Previous studies determined that these doses were non-toxic (Fry et al., 2004; Gross et al., 2014) and mice tolerated all treatments without significant body weight loss (Supplementary Figure 2B-C). Of note, animals gavaged

with the combined treatment gained less weight than the other three groups (Supplementary Figure 2D-E). Remarkably, while Palbociclib treatment alone induced a significant reduction in tumor volume compared to the control group (Figure 2A-C), the tumor growth rate of both groups was equivalent (Figure 2D-E). As a result, mice treated with Palbociclib alone did not display tumor growth inhibition (%TGI) compared to the control condition (Figure 2F). These results suggest that inhibition of CDK4/6 has only an early impact on tumor cell proliferation and that surviving cells can overcome this inhibitory effect and restore their growth. On the other hand, treatment with Telaglenestat alone failed to achieve a statistically significant reduction of tumor volume (Figure 2A-C). Nevertheless, at the end of the dosage period, tumors from mice treated with Telaglenestat exhibited a reduction in their growth rate (Figure 2D-E) and about 20% of tumor growth inhibition (Figure 2G), indicating a delayed effect of this treatment. Consistent with our *in vitro* studies, mice treated with the Palbociclib and Telaglenestat combination presented the smallest tumors (Figure 2A-C) and the slowest tumor growth rates (Figure 2D-E). These results were also confirmed by bioluminescence imaging and quantification of photon radiance (Figure 2G and Supplementary Figure 2F). In addition, we observed increasing values of tumor growth inhibition with time when Palbociclib was co-administered with Telaglenestat (Figure 2F). Likewise, tumors from mice treated with the combined therapy presented the lowest proliferative activity as determined by the quantification of mitoses (mitotic count) and KI67 labeling index, and also displayed a reduction in the levels of the angiogenic marker CD31 (Figure 2H and Suplementary Figure 2G). In contrast, compared with the control group, tumors treated with Palbociclib or Telaglenestat alone did not present any changes in the levels of these markers. A strong positive correlation between the percentage of KI67 and CD31 positive cells (Pearson $r = 0.828$, $p < 0.001$), as well as between mitotic index and KI67 (Pearson $r = 0.726$, $p < 0.01$) or CD31 (Pearson $r = 0.607$, $p < 0.04$) positive cells was reported (Supplementary Figures 2H-J). Collectively, our results reveal that the Palbociclib and

Telaglenestat combined treatment can effectively forestall acquired resistance to Palbociclib and significantly improve the efficacy of either treatment alone *in vivo*.

Metabolic features of residual tumors from *in vivo* Palbociclib and Telaglenestat treatments

Next, to determine whether the tumor cells that survived the chemotherapeutic pressures have acquired sustained features of drug resistance, we collected the residual xenograft tumors at the end of the treatments for RNA sequencing (RNA-seq) and targeted metabolite profiling analyses. A total of 268 genes were differentially expressed for Palbociclib treatment (184 downregulated, 84 upregulated), 6,028 genes for Telaglenestat (3,290 downregulated, 2,738 upregulated), and 4,774 genes for the combined treatment (2,527 downregulated, 2,247 upregulated) compared with the control group (Supplementary Figure 3A and Supplementary Table 1). Focusing on metabolic genes, 28, 580, and 500 genes were differentially expressed between the control group and tumors treated with Palbociclib, Telaglenestat, or their combination, respectively (Supplementary Figure 3B and Supplementary Table 1). In fact, metabolism was the most affected biological process after treatment with Telaglenestat alone or in combination with Palbociclib (Supplementary Figure 3C). Tumors subjected to the dual treatment presented 581 and 87 differentially expressed metabolic genes compared to Palbociclib and Telaglenestat single treatments, respectively, implying higher metabolic differences with Palbociclib than with Telaglenestat treatment (Supplementary Figure 3D and Supplementary Table 1).

Gene Set Enrichment Analysis (GSEA) (Subramanian et al., 2005) revealed a systematic decrease in the expression levels of genes associated with metabolism, cell cycle, *MYC* oncogene, and DNA repair in tumors treated with the combination (Figure 3A), and a significant enrichment for signatures associated with protein secretion and export, suggestive of cellular senescence (Hernandez-Segura et al., 2018). Over-

representation analysis (ORA) confirmed these results, showing a global reduction in the enrichment score for metabolic pathways, cell cycle, and base excision repair (Figure 3B and Supplementary Figure 4A) and a positive enrichment for senescence-related processes (Figure 3C and Supplementary Figure 4B). Consistently, the differentially expressed genes encoding enzymes of the central carbon metabolic pathways such as glycolysis, pentose phosphate pathway (PPP), tricarboxylic acid (TCA) cycle, oxidative phosphorylation (OXPHOS) and fatty acid (FA) metabolism were downregulated (Figure 3D and Supplementary Figure 5A-E). Further, the expression changes in senescence-associated genes (Supplementary Figure 5F) were in correspondence with the CellAge cellular senescence gene expression signature database (Avelar et al., 2020), indicating that the combined treatment triggers this anti-tumor mechanism leading to the irreversible arrest of cell division.

In contrast, tumors treated with Palbociclib alone displayed a positive enrichment of gene signatures related to drug metabolic mechanisms, knockdown of the PTEN tumor suppressor, activation of EGFR and KRAS signaling, epithelial-mesenchymal transition, angiogenesis, and hypoxia, and a negative correlation with gene sets associated with the cell cycle, MYC targets, pyrimidine, TCA cycle and fatty acid metabolism, and DNA replication and repair (Figure 3E and Supplementary Figures 4C-D and 5G). Together, these results describe an adaptation to Palbociclib treatment towards a more aggressive tumor phenotype that differs from the adaptive response previously reported after short *in vitro* treatments (Tarrado-Castellarnau et al., 2017). Finally, tumors from mice treated with Telaglenestat alone were negatively enriched for metabolic gene sets and exhibited an enrichment in protein secretion hallmark genes (Figure 3F-G and Supplementary Figure 4E), similarly to the dual treatment condition, while presenting increased enrichment scores for gene sets involved in the cell cycle, DNA replication and repair, and oncogenic pathways such as RAS, EGF/EGFR and PI3K (Figure 3H and Supplementary Figure 4F). These results may explain the sustained

proliferation observed in tumors treated with Telaglenestat alone, as, despite a general reduction in metabolism, they acquire additional oncogenic characteristics that maintain tumor growth.

Next, we assessed the intracellular concentrations of amino acids, biogenic amines, acylcarnitines, glycerophospholipids, and sphingolipids through targeted metabolite profiling by tandem mass spectrometry coupled to liquid chromatography (LC/MS/MS) or flow injection analysis (FIA/MS/MS). When compared to control, tumors subjected to the combined treatment exhibited lower concentrations of amino acids such as alanine, arginine, asparagine, aspartate, citrulline, glutamate, glycine, isoleucine, leucine, phenylalanine, proline, tyrosine, and valine, and an accumulation of glutamine resulting from the inhibition of glutaminase (Figure 4A). When comparing the four conditions, the lowest concentrations of amino acids, biogenic amines, and acylcarnitines were observed in the tumors subjected to dual treatment (Figure 4B and Supplementary Figure 6A), in consonance with the reduced metabolism inferred from the transcriptomic analysis. Principal component analysis confirmed that the drug combination caused the greatest aminoacidic (Supplementary Figure 6B) and lipidomic (Supplementary Figure 6C) shifts.

Conversely, we found the highest levels of phosphatidylcholines and sphingomyelins in tumors treated with the Palbociclib and Telaglenestat combination (Figure 4B and Supplementary Figure 6D-E), suggesting that cells accumulate lipids as essential components of membranes but are unable to duplicate due to the alterations of DNA synthesis, resulting in membrane remodeling. Further, in tumors treated with the drug combination, estimation of enzyme activities through metabolite ratios (Dossus et al., 2021) revealed a decrease in the activity of stearoyl CoA-desaturase (SCD) (Supplementary Figure 6F), involved in cell migration and invasion (Ran et al., 2018), and in the urea cycle and spermine synthase (SMS) of the polyamine pathway (Figure 4C-D and Supplementary Figure 6G), in line with the observed downregulation of MYC

target genes (Figure 3A) and the reduced expression of genes involved in tumor invasion and metastasis (Gerner and Meyskens, 2004). The accumulation of spermidine (Supplementary Figure 6G) is associated with autophagy induction, which suppresses proliferation and promotes apoptosis in cervical cancer cells (Chen et al., 2018), and could explain the enrichment observed in autophagic processes in tumors treated with the combination (Figure 3C).

The combined treatment also elicited a downregulation of arginine methylation (Supplementary Figure 6H) and protein arginine methyltransferases (PRMTs) (Supplementary Figure 6I), which orchestrate epigenetic modifications, chromatin architecture, transcription, signaling, splicing, DNA damage response, and cell metabolism, and are identified as promising cancer therapeutic targets (Wu et al., 2021). In fact, evaluation of the transcriptomic data from the PALOMA-2 and PALOMA-3 clinical trials for Palbociclib (Zhu et al., 2022), evidences a significant positive correlation between the expression of both *PRMT1* and *CARM1* genes and the overexpression of genes from glycolysis, OXPHOS, hypoxia, and PI3K/AKT/mTOR and MYC signaling pathways (Supplementary Figure 6J and Supplementary Table 2), which are associated with the adquisition of therapeutic resistance and shorter progression-free survival in the PALOMA-2/3 trials. Likewise, *PRMT1* and *CARM1* are positively correlated with the expression of Palbociclib resistance genes, while they are negatively correlated with the sensitivity genes identified in the PALOMA-2/3 trials comparative biomarker analyses (Zañudo et al., 2022; Zhu et al., 2022) (Supplementary Table 3). These observations suggest that residual tumor cells that survive Palbociclib therapy have acquired chemoresistance features through an epigenetic mechanism.

On the other hand, tumors subjected to the combined treatment displayed a downregulated expression of metastasis, cell cycle progression, and MYC and mTOR oncogenic pathways, as well as an increase in protein secretion and senescence pathways compared to the single treatments (Figure 4E-F). Consistently, in the tumors

treated with the combination, the expression of Palbociclib resistance genes identified in PALOMA-2/3 trials (Zañudo et al., 2022; Zhu et al., 2022) is decreased compared to Palbociclib or Telaglenestat treatments alone (Figure 4G).

Genome-scale metabolic modeling reveals that Telaglenestat is uniquely suited to counter the adaptive metabolic reprogramming induced by Palbociclib

To obtain a system-wide perspective of the metabolic reprogramming underlying treatment with Palbociclib, Telaglenestat, or their combination, we integrated the transcriptomics and metabolomics data from the residual xenograft tumors in the framework of Recon3D. Recon3D is a genome-scale reconstruction of human metabolism, providing a mathematical representation of all the reactions and transport processes known in human cells and the enzymes and transmembrane carriers mediating them (Brunk et al., 2018). More in detail, we used a quadratic multiomic metabolic transformation algorithm (qM^2TA) to impute the metabolic transformation underlying exposure to each drug and their combination by finding the intracellular metabolic flux rewiring most consistent with the transcriptomics and metabolomics measures (Figure 5A and Supplementary Figure 7A). Treatment with Palbociclib resulted in 215 reactions with a flux value increase of 25% or more relative to control, whereas 239 had their flux reduced by 25% or more. Conversely, Telaglenestat and the combined treatment resulted in a larger number of reactions with reduced flux values relative to the control, 1,461 and 1,211, respectively, whereas only 726 and 701 reactions increased their flux values by 25% or more in such treatments (Supplementary Table 4). This suggests that Telaglenestat, alone or in combination, tends to have a largely inhibitory effect on metabolism, a notion also apparent by observing the distribution of reaction flux values relative to the control (Figure 5B).

Analyzing the flux through pathways of central carbon metabolism and OXPHOS, both key for cellular proliferation and the most relevant by the magnitude of carried flux,

offers a more nuanced picture (Figure 5C and Supplementary Table 4). For instance, Palbociclib treatment caused an increased flux through oxidative phosphorylation reactions and a decreased flux through purine and pyrimidine synthesis reactions. Indeed, activation of OXPHOS can likely be attributed to increased mTOR and MYC signaling, given that both promote mitochondrial biogenesis (Cunningham et al., 2007; Morita et al., 2013; Morrish and Hockenbery, 2014). Conversely, Telaglenestat reduced the flux through the OXPHOS, glycolysis, and pentose phosphate pathways while strongly upregulating purine and, to a lesser extent, pyrimidine metabolism. Finally, the combination of Palbociclib and Telaglenestat offered the best of each individual treatment with no significant upregulation of OXPHOS and a reduced flux through the pathways of purine and pyrimidine synthesis, glycolysis, and pentose phosphate pathway.

Upregulated pathways after treatment with Palbociclib or Telaglenestat likely reflect a process of metabolic reprogramming that allows cancer cells to adapt to and counter drug-induced stress. With this in mind, we used qM^2TA to systematically search for potentially targetable enzymes or transmembrane carriers to prevent the metabolic adaptation to either Palbociclib or Telaglenestat (Supplementary Figure 7B). We identified 327 and 280 potential targets to partially revert the metabolic adaptation underlying the Palbociclib or Telaglenestat treatments, respectively (Supplementary Table 4). It is worth mentioning that glutaminase, the therapeutic target of Telaglenestat, was one of the targets against Palbociclib adaptation identified in this analysis, in accordance with our previous studies (Tarrado-Castellarnau et al., 2017). Even more remarkable, 112 targets inferred against Palbociclib adaptation, including many top-scoring targets, corresponded to genes that were significantly downregulated in response to Telaglenestat. Likewise, Palbociclib treatment downregulated 8 of the putative targets identified against Telaglenestat adaptation, including the second top-scoring putative target, ribonucleotide reductase. Given that only 15 metabolic genes

were significantly downregulated by Palbociclib, putative targets against Telaglenestat-induced metabolic adaptation were significantly overrepresented (Fisher exact test P-value = 0.01319) (Supplementary Table 5). These findings are in line with the patterns that emerged upon observation of flux changes through central carbon metabolism pathways (Figure 5C). Indeed, they reinforce the notion that Palbociclib and Telaglenestat are uniquely suited to counter the metabolic reprogramming induced by the reciprocal drug, thus providing a mechanistic rationale for the high effectiveness of the drug combination observed *in vitro* and *in vivo*.

Cells from residual tumors treated *in vivo* with Palbociclib and Telaglenestat maintain persistent drug-specific metabolic reprogramming *ex vivo*

Given that the effects of Palbociclib and Telaglenestat are time-dependent, we determined the potential persistence of their adaptive or resistant phenotypes after *in vivo* chemotherapy. To this end, we explanted 12 fresh residual tumors from mice treated for 23 days with vehicle, Palbociclib, Telaglenestat, or their combination, obtaining a total of 12 distinct two-dimensional monolayer cell cultures (three per *in vivo* treatment condition). Once established, we analyzed the glycolytic and glutaminolytic profiles of each cell line by incubation with complete media without any chemotherapeutic pressure. We found that cells derived from tumors that had been treated with the drug combination exhibited a decrease in the metabolic fluxes of glucose, glutamine, lactate, and glutamate (Figure 6A), together with a reduction in proliferation and doubling time (Figure 6B and Supplementary Figure 8A) without affecting cell cycle distribution (Supplementary Figure 8B). Likewise, the overall consumption rate of hexoses was only significantly reduced in the condition resulting from tumors treated with Palbociclib and Telaglenestat (Figure 6C). In addition, we assessed the amino acid exchange fluxes and found that alanine production, and arginine, asparagine, aspartate, histidine, isoleucine, leucine, lysine, methionine, phenylalanine, proline, and valine consumption rates were diminished in cells from tumors that had been dosed with the combination therapy

(Figure 6D and Supplementary Figure 8C). To further confirm the lower glycolytic rates observed, we measured in real-time the extracellular acidification rate (ECAR), essentially a sign of lactate production from glycolysis with a small contribution from the CO_2 produced in other reactions, while sequentially adding glucose and oligomycin to cells cultured in a medium without glucose. As expected, cells derived from Palbociclib + Telaglenestat-treated tumors portrayed a significant reduction in the glycolytic capacity, glycolytic reserve, and non-glycolytic acidification (Figure 6E). Then, we confirmed that the metabolic downregulation caused by the long-term double treatment and reported *in vivo* and 2D *ex vivo* cultures was also maintained in spheroid cultures (Figure 6F).

Considering that the TCA cycle and OXPHOS were among the gene sets downregulated *in vivo* by the treatments (Figure 3), we performed a pharmacological profiling of the mitochondrial respiratory function by combining the ATP synthase inhibitor oligomycin, the protonophoric uncoupler CCCP, the complex III inhibitor antimycin A and the complex I inhibitor rotenone, while measuring the oxygen consumption rate (OCR). This analysis revealed that cells explanted from tumors treated with the drug combination presented lower non-mitochondrial oxygen consumption, basal respiration, maximal respiration, non-ATP linked oxygen consumption (proton leak), ATP production-associated respiration, and spare respiratory capacity than control cells, depicting a global reduction in mitochondrial respiratory capacity (Figure 6G), consistent with the reported lower consumption rates of glucose and amino acids and the decrease of MYC, p-AKT, KGA and GLDH protein levels (Figure 6H). Moreover, RNA-seq analysis revealed that OXPHOS, one of the main pathways enriched during metastatic seeding and chemoresistance (Davis et al., 2020; El-Botty et al., 2023; Sica et al., 2020), was downregulated in cells derived from the combination therapy tumors compared to those obtained from control or single-agent treated tumors (Supplementary Figure 8D).

Combined Palbociclib and Telaglenestat treatment induces a less aggressive phenotype without the acquisition of resistance

Next, to compare the cellular function and energy demands of the surviving cancer cells after each chemotherapeutic treatment, we measured the ATP production rate *ex vivo* as a more accurate approach to assess the energetic cellular state than determining the total intracellular levels of ATP, which are maintained under steady-state conditions (Hardie et al., 2012). We observed that cells from tumors that were treated with the combined therapy displayed the lowest rate of mitochondrial, glycolytic, and total ATP production, while the reduction in both single-agent treatments was less pronounced (Figure 6I). Similarly, the contribution of mitochondria to oxygen consumption and proton production was significantly lower in cells previously treated *in vivo* with the combination (Supplementary Figure 8E-F), consistent with a quiescent phenotype (Figure 6J). Of note, xenograft-explanted cells presented a shift from glycolytic to mitochondrial metabolism compared to *in vitro* HCT116 cells not passaged in mice, which had an ATP rate index of 1 (Figure 6I and Supplementary Figure 8G). These results agree with the observed reduction in intracellular glutathione in cells derived from tumors treated with the combination or Telaglenestat alone (Supplementary Figure 8H), considering that this antioxidant molecule is synthesized through two ATP-requiring steps from glutamate.

To complement this analysis, we performed GSEA, which showed that cells explanted from tumors subjected to the combined therapy exhibited a downregulation of genes involved in the cell cycle machinery, MYC signaling, metastasis, OXPHOS, and electron transport chain, as compared to cells derived from tumors treated with Palbociclib alone (Supplementary Figure 8I). These cells also exhibited a downregulation of genes regulated by oncogenes such as MYC, VEGF, and cyclin D1 and associated with mitochondria and amino acid metabolism when compared with cells from tumors treated with Telaglenestat alone (Supplementary Figure 8J), revealing a persistent

reduction in the malignant potential of surviving cells that had been exposed to combined therapy *in vivo*, as compared to those subjected to a single agent.

Finally, to examine whether the xenograft-derived cell lines had shifted their sensitivity profiles after *in vivo* exposure to the therapies, we exposed the cells to increasing doses of each drug or the combination for 96 h and determined IC_{50} values. While the effect of Telaglenestat on cell proliferation was similar in all cases, regardless of *in vivo* drug exposure (Supplementary Figure 8K), *in vivo* exposure to Palbociclib alone or in combination with Telaglenestat conferred explanted tumor cells with a 2-fold increase in resistance to Palbociclib alone (Figure 6K). Remarkably, the same cells were at least as sensitive as control HCT116 cells to the combination of Palbociclib and Telaglenestat (Figure 6K). Moreover, the combination caused *in vitro* synergistic antiproliferative effects in the cell lines derived from tumors subjected to the combined therapy *in vivo* (Supplementary Table 6).

Together, these data demonstrate that long-term Palbociclib and Telaglenestat combined treatment impairs glycolytic metabolism, mitochondrial respiration, and ATP production, as well as mitigates oncogenic pathways, in colon cancer cells that survive *in vivo* therapy with both drugs, resulting in a persistently less aggressive tumor phenotype.

Discussion

Targeting cell cycle through cyclin-dependent kinases 4 and 6 (CDK4/6) inhibition is a promising strategy in cancer therapy since they play a major oncogenic role in a wide range of human cancers (Goel et al., 2022). However, like with all targeted therapies, tumor cells eventually acquire resistance to CDK4/6 inhibition (Papadimitriou et al., 2022). Therapeutic resistance is currently one of the most critical challenges in cancer treatment. Under environmental pressures such as a chemotherapeutic treatment,

cancer cells engage adaptive mechanisms to optimize survival, therefore becoming resistant (Labrie et al., 2022). Metabolic reprogramming is one of these relevant cell-autonomous mechanisms through which tumor cells change their energetic dependencies to alternative pathways to bypass the selective pressures exerted by a given class of antineoplastic drugs (Mendez-Lucas et al., 2020; Pranzini et al., 2021). This metabolic shift constitutes adaptive responses that reveal vulnerabilities that can be targeted through combination therapies to prevent and overcome chemoresistance (El-Botty et al., 2023). Our study integrates metabolomics and transcriptomics data to describe the adaptation undergone by tumor cells after CDK4/6 and glutaminase inhibition, both *in vitro* and *in vivo*, to predict the best targets for combination therapy and compare its suitability versus the single treatments.

Numerous pre-clinical studies and clinical trials are currently exploring the therapeutic potential of combining CDK4/6 inhibitors with endocrine therapies (e.g., aromatase inhibitors, fulvestrant), immunotherapies (e.g., antibodies to PD1/PD-L1), oncogenic kinase inhibitors (e.g., receptor tyrosine kinase-PI3K-AKT-mTOR signaling, RAS, BRAF, MEK, IGF-1R, ALK inhibitors), and other targeted or chemotherapeutic agents (e.g., autophagy, PARP inhibitors) in solid tumors (Goel et al., 2022). Our previous work identified the inhibition of glutaminase as the best metabolism-based strategy to combine with CDK4/6 targeting therapy (Tarrado-Castellarnau et al., 2017) and was later corroborated by other studies in esophageal squamous cell carcinoma (Qie et al., 2019) and lung cancer (Conroy et al., 2020). In our prior studies, we found that Palbociclib, a selective small-molecule inhibitor approved for the treatment of HR-positive HER2-negative locally advanced or metastatic breast cancer (Dhillon, 2015), caused an accumulation of MYC protein levels, which ultimately resulted in glutamine addiction, rendering tumor cells highly sensitive to inhibitors of glutaminase such as Telaglenestat (Tarrado-Castellarnau et al., 2017), an orally bioavailable selective

inhibitor of both glutaminase 1 isoforms (KGA and GAC) (Gross et al., 2014; Harding et al., 2021).

In this work, we have confirmed that the combinatorial targeting of CDK4/6 and glutaminase with Palbociclib and Telaglenestat causes synergistic antiproliferative effects on HCT116 colon cancer cells *in vitro*, together with a decrease in MYC accumulation compared to the single treatments. We observed that the metabolic reprogramming undergone by cancer cells after these treatments was time-dependent, but the synergetic antiproliferative effect of the dual treatment was independent of time and effective both *in vitro* and *in vivo*. In contrast, the inhibition of glutaminase alone did not cause a significant decrease in tumor volume. Likewise, tumors administered with Palbociclib single treatment had the same growth rate as the control tumors despite exhibiting a significant reduction in their volume, suggesting that Palbociclib activity is time-dependent and that, after the initial antiproliferative effect, surviving tumor cells acquire the capacity to overcome this inhibition and restore their proliferative rate. The combined inhibition of CDK4/6 and glutaminase caused the greatest significant tumor growth inhibition, together with the lowest proliferative and angiogenic activities, thus preventing cell reprogramming and the acquisition of chemoresistance. In fact, tumors subjected to dual therapy presented a decrease in the expression of Palbociclib-resistance genes identified in PALOMA-2/3 trials (Zañudo et al., 2022; Zhu et al., 2022). In addition, the combination treatment triggered the downregulation of arginine methylation and protein arginine methyltransferases (PRMTs). PRMTs expression correlates with the activation of resistance pathways associated with lower progression-free survival (Zhu et al., 2022) and is upregulated through MYC and mTORC1 activation (Litzler et al., 2023), suggesting that Palbociclib-surviving cells might have acquired chemoresistance through an epigenetic mechanism. Moreover, gene set enrichment analysis confirmed that tumors subjected to the double therapy exhibited a

downregulation in metastasis, cell cycle progression, and MYC and mTOR oncogenic pathways, consistent with the downregulation of PRMTs observed (Litzler et al., 2023).

Metabolic reprogramming is a systems-level property emerging from the complex interaction between enzymes and metabolites. Here, we used qM^2TA to integrate the metabolite and enzyme transcript levels and analyze the genome-scale metabolic rewiring arising from treatment with Palbociclib, Telaglenestat, or their combination *in vivo*. From this analysis, it emerged that Palbociclib treatment resulted in increased flux through OXPHOS, attributable to increased mTOR and MYC signaling (Cunningham et al., 2007; Morita et al., 2013; Morrish and Hockenbery, 2014), and decreased flux through reactions involved in nucleotide synthesis. Our observations are in line with recent findings describing that the treatment of metastatic breast cancer with Palbociclib elicits increased OXPHOS as a resistance mechanism that can be countered pharmacologically (El-Botty et al., 2023). In contrast to Palbociclib, Telaglenestat treatment decreased flux through OXPHOS, glycolysis, and the pentose phosphate pathway, while increasing flux through nucleotide metabolism. Notably, nucleotide synthesis, pentose phosphate pathway, glycolysis, and TCA play a key role in the synthesis of biomass building blocks needed for proliferation and are commonly upregulated in cancer compared to healthy tissue (Tarrado-Castellarnau et al., 2016). On the other hand, OXPHOS is often upregulated in cancer stem cells and drug-resistant tumors (Davis et al., 2020; Sica et al., 2020), also in Palbociclib-resistant patient-derived xenografts of HR-positive metastatic breast cancers (El-Botty et al., 2023). Hence, the combination of Palbociclib and Telaglenestat maintained the benefits of each individual treatment while sparing upregulation of OXPHOS as a resistance mechanism and reducing flux through nucleotide synthesis, glycolysis, and pentose phosphate pathways. This was further confirmed when we identified that many of the putative targets against the metabolic adaptation to Palbociclib were downregulated by Telaglenestat and vice versa. Therefore, our analysis indicates that Palbociclib and Telaglenestat are ideal for

countering the metabolic reprogramming induced by their respective single treatments, mechanistically explaining the high efficiency of the combined therapy both *in vitro* and *in vivo*. Our study also suggests a promising new strategy for searching for inhibitors against chemoresistance where, rather than searching for inhibitors targeting only one upregulated pathway, drugs capable of inhibiting multiple resistance-associated pathways should be sought.

We also confirmed that the drug-specific metabolic reprogramming of surviving cancer cells after *in vivo* treatments was maintained in *ex vivo* cultures in the absence of chemotherapeutic pressure. Specifically, cells derived from tumors treated with the combination of Palbociclib and Telaglenestat presented a general decrease in the central carbon metabolic fluxes in conjunction with an overall reduction in mitochondrial respiration as well as in mitochondrial, glycolytic, and total ATP production. In addition, these cells displayed diminution in the enrichment of oncogenic pathways compared to cells from tumors subjected to Palbociclib or Telaglenestat alone, indicating a less malignant phenotype, and did not present acquired resistance to the double treatment *in vitro* in contrast with Palbociclib single agent.

In conclusion, this study demonstrates that targeting the compensatory metabolic pathway of glutaminolysis after CDK4/6 inhibition is a uniquely suitable combinatorial intervention to prevent Palbociclib resistance in colon cancer and reduce tumor growth *in vivo*.

Methods

Compounds and reagents

Palbociclib (PD0332991) and Telaglenestat (CB-839) were purchased from Selleckchem (Houston, TX, USA). The glutaminase inhibitor bis-2-(5-phenylacetamido-1,2,4-thiadiazol-2-yl)ethyl sulfide (BPTES) was kindly provided by Dr. Mariia Yuneva (The Francis Crick Institute, London, UK). Stock solutions of 10 mM were prepared with water or dimethyl sulfoxide (DMSO) according to the manufacturer's instructions. Antibiotics (10,000 U/ml penicillin, 10 mg/ml streptomycin), PBS, and Trypsin EDTA solution C (0.05% trypsin – 0.02% EDTA) were obtained from Biological Industries (Kibbutz Beit Haemet, Israel), and fetal bovine serum (FBS) from Invitrogen (Carlsbad, CA, USA).

Cell culture

The human colorectal carcinoma cell line HCT116 and the human embryonic kidney 293T (HEK293T) cells were obtained through the American Type Culture Collection (ATCC, Manassas, VA, USA). The HCT116 derivative $HCT116^{Luciferase\text{-}GFP}$ cells were obtained through lentiviral transfection and transduction. Twelve HCT116 derivative cell lines were obtained from tumors from mice that had been treated daily with vehicle, Palbociclib, Telaglenestat, or the combination of Palbociclib and Telaglenestat for 23 days (three independent cell lines per condition). All cell lines were grown in the absence of chemotherapeutics. HCT116 cells and all the derivative cell lines were cultured in Dulbecco's modified Eagle medium (Gibco, Thermo Fisher Scientific Inc., Waltham, MA, USA) / Nutrient mixture HAM F12 (Biological Industries) (DMEM/F12, 1:1 mixture) with 2.5 mM L-glutamine and 12.5 mM D-glucose. HEK293T cells were cultured in DMEM culture medium. Media were supplemented with 10% FBS, penicillin (50 U/ml), and streptomycin (50 µg/ml). Cells were incubated at 37ºC in a humidified atmosphere with 5% CO_2. All cell lines were regularly tested for mycoplasma contamination and cultivated for less than three months after receipt, generation, or thawing.

Lentiviral transfection and transduction

HEK293T cells were transiently transfected using Fugene reagent (Roche, Indianapolis, IN, USA) with pCMV-GFP/Luc plasmid (kindly provided by Dr. Timothy M. Thomson) for the constitutive co-expression of the firefly luciferase gene and GFP. Viral supernatants were harvested 48 h after transfection, filtered through 0.45 µm methylcellulose filters (Merck Millipore, Billerica, MA, USA), and used to transduce HCT116 recipient cells. 5×10^5 HCT116 cells were cultured in the presence of the viral supernatant and 8 µg/ml polybrene for 24 h. GFP-positive transduced cells were selected by fluorescence-activated cell sorting (FACS) (MoFlo, Beckman Coulter). Luminescence levels yielded by cell lysates were measured using the Luciferase Assay System kit (Promega, Madison, WI, USA) in a Mithras LB 940 plate reader (Berthold Technologies, Bad Wildbad, Germany).

Cell proliferation assays

Having optimized the seeding density, 2×10^3 cells per well were seeded in 96-well plates, and media were replaced at 24 h with fresh media containing different concentrations of each drug, the combination of drugs, or vehicle. Plates were placed in an IncuCyte® S3 (Sartorius, Göttingen, Germany) live-cell analysis system to monitor cell confluence. At 96 h, cells were washed with PBS and lysed with 0.01% SDS, and plates were stored frozen at -20 ºC overnight. Then, plates were thawed at 37 ºC and incubated in darkness with 4 µg/ml Hoechst (HO33342; 2'-[4-ethoxyphenyl]-5-[4-methyl-1-piperazinyl]-2,5'-bi-1H-benzimidazole trihydrochloride trihydrate, Sigma-Aldrich, St Louis, MO, USA) DNA stain in solution buffer (1 M NaCl, 1 mM EDTA, 10 mM Tris-HCl pH 7.4) on a shaker at 37 ºC for 1 h. Finally, fluorescence was measured in a FLUOstar OPTIMA microplate reader (BMG LABTECH GmbH, Ortenberg, Germany) at 355 nm excitation and 460 nm emission. Cell proliferation was represented as a percentage relative to untreated control cells. Concentrations that caused 50% of inhibition of cell proliferation (IC_{50}) were

calculated using GraphPad Prism 7 software (GraphPad Software, San Diego, CA, USA). Cell size and volume values were obtained using a Scepter™ Handheld Automated Cell Counter (EMD Millipore Corporation, Billerica, MA), which employs the Coulter principle of impedance-based particle detection.

Dose-response assays and combination index determination

Drug synergies were evaluated with the CompuSyn software (ComboSyn, Inc., Paramus, NJ, USA). The effectiveness of the combined drug treatments was quantified by determining the Combination Index (CI), where CI<1, CI=1, and CI>1 indicate synergism, additivity, and antagonism, respectively (Chou and Talalay, 1984).

Colony formation assays

Single-cell suspensions of $1x10^3$ cells per well were seeded in 6-well plates and treated after 24 h with either vehicle, single drugs, or their combination. Colonies are allowed to grow for ten days and then fixed and stained with 0.5% (w/v) Crystal Violet (Sigma-Aldrich) in 20% methanol. Image acquisition with ImageJ software (public domain National Institutes of Health, USA, http://rsbweb.nih.gov/ij/) was used to score the number of colonies.

Spheroid assays

A total of $1x10^4$ cells were seeded in 24-well ultra-low attachment culture plates (Corning, NY, USA) in the presence of the specified inhibitor(s) in serum-free media supplemented with 20 ng/ml EGF (Gibco), 20 ng/ml bFGF (Gibco), 10 µg/ml heparin (Sigma-Aldrich), 1:50 (v/v) B-27 supplement 50x (Gibco), 5 µg/ml insulin solution human (Sigma-Aldrich) and 0.5 µg/ml hydrocortisone (Sigma-Aldrich). At the end of the experiment, spheroids were incubated with 0.5 mg/ml 3-(4,5-dimethylthiazol-2-yl)-2,5-diphenyltetrazolium bromide (MTT, Sigma-Aldrich) for 2-3 h until fully stained. Plates were scanned,

spheroids were scored, and spheroid area and volume were quantified by image acquisition with ImageJ software.

Cell cycle analysis

Cells were collected by centrifugation after trypsinization, resuspended in PBS, and fixed dropwise with 70% (v/v) cold ethanol for at least 2 h. Then, cells were centrifuged, washed twice with PBS, resuspended in PBS containing 0.2 mg/ml DNAse free RNAse A (Roche, Basel, Switzerland), and incubated for 1 h at 37ºC. Prior to analysis, 50 µg/ml propidium iodide (PI) was added. Samples were analyzed using a Gallios multi-color flow cytometer instrument (Beckman Coulter, Brea, CA, USA) set up with the 3 lasers 10 colors standard configuration. Excitation was done with a blue (488 nm) laser. Forward scatter (FS), side scatter (SS), red (620/30 nm) fluorescence emitted by PI were collected. Red fluorescence from PI was projected on a 1,024-channel monoparametric histogram. Aggregates were excluded by gating single cells by their area vs. peak fluorescence signal. DNA analysis (ploidy analysis) from 10^4 cells on single fluorescence histograms was done using MultiCycle software (Phoenix Flow Systems, San Diego, CA, USA).

Western blot analysis

Cells were washed twice with ice-cold PBS and incubated for 30 min on ice with RIPA buffer containing 50 mM Tris (pH 8.0), 150 mM sodium chloride, 1% Triton X-100, 0.5% sodium deoxycholate, 0.1% sodium dodecyl sulfate (SDS), 1% protease inhibitor cocktail set III and 1% phosphatase inhibitor cocktail set IV (EMD Millipore Corporation). Cells were scraped, sonicated, and centrifuged at 12,000 g for 20 min at 4ºC. Supernatants were recovered, and the protein content was quantified with the BCA kit (Pierce Biotechnology).

Equal amounts of protein per sample were size-separated by electrophoresis on SDS-polyacrylamide gels and electroblotted onto Immobilon®-P polyvinylidene fluoride

(PVDF) transfer membranes 0.45 µm pore size (Merck Millipore Ltd., Cork, IRL). After 1 h of blocking at room temperature with 5% skim milk in PBS 0.1% Tween, blots were incubated with the specific primary antibodies overnight at 4ºC. Then, membranes were treated with the appropriate horse radish peroxidase (HRP)-labeled secondary antibody for 1 h at room temperature. All blots were treated with Immobilon® Western Chemiluminescent HRP Substrate (EMD Millipore Corporation, Burlington, MA, USA) and developed after exposure to an autoradiography film (VWR International, Radnor, PA, USA). The primary antibodies used were Phospho-Akt (#9271), mTOR (#2972), and Phospho-mTOR (#5536) from Cell Signaling (Beverly, MA, USA); GLS1 (ab93434), GLUD (ab166618) and MYC (ab32072) from Abcam (Cambridge, UK); GAC (19958-1-AP) and KGA (20170-1-AP) from Proteintech (Chicago, IL, USA); HIF1α (sc-13515) from Santa Cruz Biotechnology; and β-actin (#69100) form MP Biomedicals (Santa Ana, CA, USA). The secondary antibodies used were anti-mouse (ab6728) and anti-rabbit (ab6721) from Abcam.

Measurement of extracellular metabolites

Media samples were collected at the beginning and the end of the incubation and frozen until analyzed. At the same time points, cell number was determined for normalization purposes. All the biochemical assays were carried out under exponential growth conditions. Glucose, lactate, glutamate, and glutamine concentrations from cell culture media were determined using a COBAS Mira Plus spectrophotometer (HORIBA ABX Diagnostics, Kyoto, Japan) to monitor the production of NAD(P)H in specific reactions for each metabolite at 340 nm wavelength. Glucose concentration was measured using hexokinase and glucose-6-phosphate dehydrogenase coupled enzymatic reactions (ABX Pentra Glucose HK CP, HORIBA ABX, Montpellier, France). Lactate concentration was determined at 37 ºC with 2.35 mg/ml NAD^+ (Roche) in 0.15 M hydrazine 10.9 mM EDTA pH 9 buffer and 80 U/ml lactate dehydrogenase (Roche) in 51 mM ammonium sulfate pH 6.5 buffer. Glutamate concentration was assessed at 37 ºC with 2.08 mM

ADP, 3.35 mM NAD^+, and 16 U/ml of glutamate dehydrogenase (Roche) in 0.28 M glycine / 0.35 M hydrazine / 1.12 mM EDTA pH 9 buffer. Glutamine concentration was calculated through its conversion to glutamate at 37 ºC for 30 min with 100 mU/ml glutaminase in 0.1 M acetate pH 5 buffer and subsequently quantifying glutamate concentration as described above.

Estimation of metabolite consumption and production rates

Net fluxes per cell of uptake and release of different metabolites (J_{met}) were estimated from the experimentally measured variations of metabolite concentration in medium and cell number for 24 h. The estimation was performed by assuming exponential growth and constant uptake or release per cell, which corresponds to a simple model of cell growth and metabolite consumption/production:

$$\frac{dN_t}{dt} = N_t \times \mu \qquad \frac{dM_t}{dt} = N_t \times J_{met}$$

Where *N* is cell number, *M* is the quantity of metabolite, and *μ* growth rate.

Total glutathione quantification

Fresh cells were lysed with 5% 5-sulfosalicylic acid solution, vortexed, and disrupted by two freezing/thawing cycles in liquid nitrogen and a 37 ºC water bath. Cell extracts were incubated at 4 ºC for 10 min and centrifuged at 10,000 g for 10 min. The reaction was initiated by mixing 150 µl of working solution (15 U/ml of glutathione reductase and 40 µg/ml of 5,5'-Dithiobis(2-nitrobenzoic acid) in 100 mM K_2HPO_4/KH_2PO_4 1 mM EDTA pH 7.0 buffer) with 10 µl of cell extract (diluted 1:5 or 1:10) or oxidized glutathione standards (from 0 to 12.5 µM). Then, 50 µl of 0.16 mg/ml NADPH solution were added to the samples, and the increase in absorbance with time was measured at 340 nm wavelength. Total glutathione concentration was normalized by protein content.

Mouse xenografts and in vivo drug studies

Animal experiments were carried out at the Parc Científic de Barcelona - Parc de Recerca Biomèdica de Barcelona (PCB-PRBB) Animal Facility Alliance, in compliance with current regulations (RD 53/2013; Directive 2010/63/UE; Decree 214/1997/GC, Order ECC/566/2015), to ensure that animal experiments are conducted in a humane and ethical manner. The protocol for this study was approved by the PCB's Animal Experimentation Ethics Committee and the Animal Experimentation Commission of the Generalitat de Catalunya.

Palbociclib isethionate (S1579, SelleckChem) was resuspended at 50 mg/ml in 50 mM sodium L-lactate (Sigma-Aldrich) pH 4 buffer. Telaglenestat (S7655, SelleckChem) was dissolved at 50 mg/ml in 10 mM sodium citrate (Sigma-Aldrich) pH 2 buffer with 25% w/v (2-hydroxypropyl)-β-cyclodextrin (HP-β-CD, Sigma-Aldrich). Treatments were aliquoted into single and combined daily doses and frozen at -80 ºC. HCT116$^{Luciferase\text{-}GFP}$ cells, after a test for mycoplasma contamination, were resuspended in sterile PBS and injected (10^6 cells in 100 µl) subcutaneously on the right flank of anesthetized 5-week-old male non-obese diabetic severe combined immunodeficiency disease (NOD-SCID) mice (strain: NOD.CB17/AlhnRj-Prkdcscid; type: Mutant congenic mouse; Janvier Labs, Le Genest-Saint-Isle, France). Tumor growth was monitored three times a week by non-invasive bioluminescence on an IVIS® Spectrum In Vivo Imaging System (PerkinElmer, Waltham, MA, USA). Images and radiance were acquired 10 min after intraperitoneal injection of 150 µl of 100 mg/kg D-luciferin (BioVision Inc, Waltham, MA, USA) in sterile PBS. Eight days after tumor cells implantation, mice were randomly distributed in 4 treatment groups of fourteen animals each and administered via oral gavage with daily doses of vehicle, 100 mg/kg/day Palbociclib, 150 mg/kg/day Telaglenestat, or 100 mg/kg/day Palbociclib + 150 mg/kg/day Telaglenestat for 23 consecutive days. Mice were weighed every three days to readjust the treatment volume for precise drug dosing. Average radiance (photons (p)/s/cm^2/steradian (sr)) was calculated for each mouse using a circular region of interest with the mouse in a prone position and normalized to the value obtained at

the same area before starting treatment administrations (day 8) using the IVIS® Spectrum Living Image® 4.3.1 software (PerkinElmer). Tumor growth was also monitored thrice a week from day 15 by measuring tumor volume with a Vernier caliper using the modified ellipsoid volume formula: Tumor volume (mm^3) = (length × $width^2$) × π/6. Tumor growth inhibition (TGI) rate was calculated as TGI = $(1-(V_{(T,t)}/V_{(T,0)})/(V_{(C,t)}/V_{(C,0)}))$ x 100 (Li et al., 2019), where time 0 is the first measurement of tumor volume on Day 15. At the end of the treatment, mice were euthanized, and the tumors were collected for further analysis. Animals were allowed to form tumors up to 1.5 cm in diameter, at which point they were euthanized.

Cell line generation *ex vivo*

Three tumors for each treatment group were excised, placed in Petri dishes with DMEM/F12 medium, cut into fragments with a sterile scalpel, and subjected to digestion with 1 mg/ml collagenase type IV (Sigma-Aldrich) for 30 min at 37 ºC under aseptic conditions. Then, tissue was centrifuged and digested with Trypsin EDTA solution C to generate a single cell suspension, filtered through a 40 µm cell strainer, and plated in DMEM/F12 with 2.5 mM L-glutamine, 12.5 mM D-glucose, 10% FBS, penicillin (50 U/ml), and streptomycin (50 µg/ml), obtaining twelve independent cell lines (three for each treatment condition).

Immunohistochemistry (IHC) staining of mouse xenograft tissues

Mouse xenografts were dissected immediately after surgical resection. Three tumors for each treatment condition were fixed in 4% paraformaldehyde (PFA) and paraffin-embedded in blocks for histology assessment. Serial 4-µm tumor sections were obtained from the PFA-fixed, paraffin-embedded tumor tissues by microtome cuts. Immunohistochemistry staining was performed by the Francis Crick Institute (UK) Experimental Histopathology Laboratory on the Discovery Ultra Ventana platform (Roche). The antibody dilutions of 1:750 for CD31 (ab182981, Abcam) and of 1:1000 for

KI67 (ab15580, Abcam) were used, with antigen retrieval using Cell Conditioning 1 (CC1, Roche) for 48 minutes and primary antibody incubation for 60 minutes. All slides were counterstained with Harris hematoxylin nuclear stains (Leica Biosystems, Wetzlar, Germany), dehydrated, cleared, and mounted in a Tissue-Tek Prisma® automated slide stainer (Sakura Finetek, Torrance, CA, USA). Slides were imaged on the Zeiss Axio Scan.Z1 slide scanner (Carl Zeiss Microscopy GmbH, Jena, Germany), and the percentage of KI67 and CD31 positive cells was evaluated using QuPath version 0.4.2 (Bankhead et al., 2017). A board-certified pathologist (A.S-B.) assessed the mitotic index by counting mitoses in 10 high power fields (HPF, 400×) on hematoxylin and eosin (H&E)-stained tumor sections.

RNA sequencing

Total RNA was isolated using the RNeasy mini kit (Qiagen, Hilden, Germany) following the manufacturer's instructions and including a DNase (Qiagen) digestion step. The size, concentration, and integrity of total RNA were determined by electrophoresis in a 4200 TapeStation system (Agilent, Santa Clara, CA, USA). Whole transcriptome sequencing (RNA-Seq) was performed at the Genomics Unit of CNIC (National Centre for Cardiovascular Research, Madrid, Spain). Barcoded RNA-Seq libraries were prepared with 200 ng of total RNA with RIN > 8 using the NEBNext® Ultra™ RNA Library Prep Kit for Illumina (New England Biolabs, Ipswich, MA, USA). Poly A+ RNA was purified using poly-T oligo-attached magnetic beads followed by fragmentation and first and second cDNA strand synthesis. The second strand was synthesized with uracil instead of thymine. Then, cDNA 3′-ends were adenylated, adapters were ligated, uracils were excised, and the libraries were amplified by PCR. The size of the libraries was determined using a 2100 Bioanalyzer DNA 1000 chip (Agilent), and their concentration was calculated using the Qubit® fluorometer (Life Technologies). All samples were indexed, and multiplex sequencing was conducted on a HiSeq2500 instrument (Illumina, San Diego, CA, USA) to generate 60-base reads in single-end format. FastQ files for

each sample were obtained using CASAVA v1.8 software (Illumina). Reads were aligned to the Ensembl reference genome and converted to reads per gene with the STAR software.

Gene expression analysis

The DESeq2 package for R was applied to normalize gene counts and identify differentially expressed genes across the study conditions (Love et al., 2014). Gene Set Enrichment Analysis (GSEA) was also used to infer enriched gene signatures from the Molecular Signatures Database (MSigDB) (Subramanian et al., 2005). The normalized enrichment score (NES) was used to rank the enriched gene sets in each phenotype. A false discovery rate q-value (FDR q-value) was computed to estimate the probability that a gene set with a given NES represented a false positive finding. Over-representation analysis (ORA) was applied to determine the biological functions or processes enriched in the differentially expressed genes of each treatment condition using WebGestalt (Liao et al., 2019).

Normalized Gene expression data from PALOMA2 (GSE133394) and PALOMA3 (GSE128500) was obtained from the GEO repository. The R package ssGSEA2 (sample Gene Set Enrichment Analysis 2) was used to compute the gene sets enrichment in each sample (Krug et al., 2019). The following sets from the Human Molecular Signatures Database (Liberzon et al., 2011) were used: HALLMARK MTORC1 SIGNALING, HALLMARK G2M CHECKPOINT, HALLMARK FATTY ACID METABOLISM, HALLMARK HYPOXIA, HALLMARK E2F TARGETS, HALLMARK GLYCOLYSIS, HALLMARK OXIDATIVE PHOSPHORYLATION, HALLMARK IL2 STAT5 SIGNALING, HALLMARK PI3K AKT MTOR SIGNALING, HALLMARK MYC TARGETS V1 and HALLMARK MYC TARGETS V2. The cor.test function from R was used to evaluate the Pearson Correlation between *PRMT* genes expressed in PALOMA2/3 samples (*CARM1*

and *PRMT1*) and pathway enrichment scores and expression levels of Palbociclib-resistance genes (Zañudo et al., 2022; Zhu et al., 2022).

Targeted metabolomics

Intracellular metabolites were extracted from tumors frozen in dry-ice cooled isopentane with 85:15 EtOH:PBS buffer and then sonicated 3 times for 5 seconds each, submerged in liquid nitrogen for 30 seconds, and thawed at 95 ºC twice. Then, extracts were centrifuged at 20,000 g for 5 minutes at 4ºC, supernatants were collected, and protein content was determined. Cell media were collected at the beginning and the end of a 24-hour incubation in exponential growth, and cell number was determined for normalization purposes. Extracts from tumors and media were analyzed using the Absolute IDQ p180 kit (Biocrates Life Sciences AG, Innsbruck, Austria) with an Agilent 1290 Infinity UHPLC system (Agilent, Santa Clara, CA, USA) coupled with an MS/MS Sciex Triple Quad 6500 (AB Sciex LLC, Framingham, MA, USA) according to the manufacturer's instructions. Data analysis was performed using Analyst (AB Sciex LLC) and MetIDQ™ (Biocrates Life Sciences AG) software. A total of 21 amino acids, 21 biogenic amines, 40 acylcarnitines, 90 glycerophospholipids, 15 sphingolipids, and hexose sugars were analyzed. Data were normalized by cell number for media samples and protein for tumor samples. Clustering, heatmaps, and statistical analysis were performed using MetaboAnalyst 5.0 (Pang et al., 2022).

Cellular bioenergetics

XFe24 Extracellular Flux Analyzer (Seahorse Bioscience, North Billerica, MA, USA) was used to measure the oxygen consumption, extracellular acidification, and proton efflux rates (OCR/ECAR/PER) in media immediately surrounding adherent cells cultured in an XFe24-well microplate (Seahorse Bioscience). One day before analysis, $7x10^4$ cells were plated in a monolayer in 100 µl, adding 150 µl of complete medium 4 h later, once cells were attached, and incubated at 37 ºC and 5% CO_2 overnight. Then, growth media

were replaced by basal media (unbuffered DMEM, pH 7.4; Sigma-Aldrich) with or without glucose and incubated at 37ºC for 1 h without CO_2. The sensor cartridge was hydrated with calibration solution (Seahorse Bioscience) overnight at 37 ºC and loaded with the test reagents into the Seahorse Analyzer to calibrate the sensors. Mitochondrial function and potential were analyzed by sequential injection of 1 μM oligomycin (ATP synthase inhibitor; Sigma-Aldrich), 0.6 μM Carbonyl Cyanide m-Chlorophenylhydrazone (CCCP, mitochondrial uncoupler; Sigma-Aldrich) together with 2 mM pyruvate to achieve maximal respiration, and 2 μM rotenone and antimycin A (mitochondrial complex I and III inhibitors, respectively; Sigma-Aldrich). Cells were counted at the end of the experiments to normalize the OCR, ECAR, and PER readings. Respiration, acidification, and ATP production rates were calculated following the Agilent Seahorse XF Technology instructions.

Building condition-specific metabolic models

Condition-specific genome-scale metabolic models (GSMMs) for control and residual tumors from *in vivo* Palbociclib and Telaglenestat treatments were reconstructed from the human GSMM Recon3D (Brunk et al., 2018). Recon3D describes the metabolic potential of the human genome, yet in any given condition, only a subset of enzymes is expressed. Hence, we reconstructed condition-specific GSMMs containing only enzymes expressed in the study conditions. More in detail, enzymes with fragments per kilobase of exon per million mapped fragments (FPKM) under 1 in all conditions were removed, provided that their removal still enabled the models to produce 50% of optimal biomass as well as the synthesis or uptake of all amino acids and biogenic amines detected with the metabolomics assays. Additionally, enzymes that were expressed below 1 FPKM in a given treatment but not in control were also removed from the treatment-specific model if the difference in gene expression to the control was statistically significant (FDR adjusted P value <0.05).

Quadratic multiomic metabolic transformation algorithm (qM^{2}TA)

The quadratic multiomic metabolic transformation algorithm (qM^{2}TA) models a metabolic transition between two states by maximizing the consistency between gene expression and metabolomics data and reaction fluxes (Figure 5A, Supplementary Figure 7). It allows the integration of both transcriptomics and metabolomics fold changes weighted by their statistical significance across both states and can identify key targets to revert the metabolic transformation.

To run qM^{2}TA, we first computed the flux distribution in the control tumors condition (v_i^{ref}, reference flux distribution) by applying the GIME3 algorithm (Schmidt et al., 2013). Briefly, this algorithm consists of a flux minimization weighted by gene expression subject to achieving 95% of the maximum biomass production and producing all measured metabolites. Next, flux variability analysis (Gudmundsson and Thiele, 2010) is used to identify the solution space within 99% of the GIME3 optimal solution. Finally, the resulting solution space is sampled using the Artificial Centering Hit-and-Run algorithm implemented into COBRApy (Ebrahim et al., 2013; Heirendt et al., 2019). The average of these flux samples is used as the control/reference flux distribution.

Then, qM^{2}TA optimization is used to simulate the metabolic transition upon treatment by maximizing the consistency between gene expression and metabolite concentration fold changes and simulated reaction flux fold changes relative to the control. The optimization minimizes the difference between the resulting flux values and target flux (i.e., the product of reference flux value by fold change) for each differentially expressed metabolic gene or metabolite concentration. To give more weight to the features with more statistically significant differences, each feature (metabolite level or gene expression measure) is given a weight to the minimization inversely proportional to the P-value for the hypothesis that the fold change is different from 1. Additionally, flux variation is minimized for reactions not associated with differentially expressed genes or

metabolites. The reference flux distribution scales both terms of the optimization to prevent a bias towards reactions with high reference flux.

$$min \sum_{m \in DExp} \left(W_m \sum_{i \in R_m} \left(\frac{v_i^{ref} \cdot FC_m - v_i^{res,qM^2TA}}{v_i^{ref}(FC_m - 1)} \right)^2 \right) + \sum_{i \in Ru} \frac{\left(v_i^{ref} - v_i^{res,qM^2TA}\right)^2}{v_i^{ref}}$$

$$W_{gm} = LOG10(p_{th}) - LOG10(p_m)$$

Subject to

s. v^{res,qM^2TA}*=0*

$$lb < v^{res,qM^2TA} < ub$$

Where:

$DExp$ is the list of differentially expressed genes and differentially abundant metabolites between the control and a target condition.

W_m is the weight given to measure m.

R_m are the reactions associated with measure m. For genes, this information is taken from the gene-reaction rules defined in Recon3D. Metabolomics measures are mapped to a sink reaction consuming the measured metabolite.

v_i^{ref} is the reference flux value (i.e., computed for the control condition) for reaction i.

FC_m is the gene expression or metabolite concentration fold change relative to the control.

v_i^{res,qM^2TA} is the simulated flux value for reaction *i* in the condition of interest.

Ru are the reactions not associated with any differentially expressed genes.

s is the stoichiometric matrix of the condition-specific GSMMs. The product of such matrix with v^{qM^2TA} is set to 0 to define the steady-state constraint (i.e., inputs and outputs fluxes for each metabolite must be balanced).

lb and *ub* define reaction flux lower and upper bounds, respectively. For reactions identified as inactive when building condition-specific GSMMs, both *lb* and *ub* will be 0, preventing the reaction from carrying any flux. To simulate the effect of the glutaminase inhibitor, in the samples dosed with Telaglenestat or with the combination of Palbociclib and Telaglenestat, the maximum flux through glutaminase reaction (*ub*) was constrained to a maximum value of half the reference flux (v_i^{ref}).

W_g is the weight given to each measured gene or metabolite.

p_{th} is the p-value threshold used to define a fold change in gene expression or metabolite levels as differentially expressed. The threshold was defined as 0.25 FDR-adjusted p-value.

p_m is the FDR-adjusted p-value for measure m for the fold change between the condition under study and the control.

Comparing the flux values simulated in a given treatment (v_i^{res,qM^2TA}) to those in control (v_i^{ref}) can yield a unique insight into the metabolic reprogramming underlying the adaptation to the treatment-induced stress. Reactions were grouped into metabolic pathways to facilitate interpreting the results, and the fold changes of total flux values through each pathway relative to the control were computed. Reactions were assigned to metabolic pathways based on KEGG annotations for the genes catalyzing them.

Similar to MTA and rMTA (Valcarcel et al., 2019; Yizhak et al., 2013), qM^{2}TA can identify gene targets that can disrupt a particular metabolic transformation, in this case, the metabolic adaptation to Palbociclib or Telaglenestat. The potential of each metabolic

gene to impede such metabolic transformation is evaluated by systematically running qM^{2}TA while reducing the maximum flux (*ub*) of reactions catalyzed by a given gene to 50% of the flux value in the control condition (v_i^{ref}). This enables testing each gene's capacity to facilitate or disrupt the metabolic transformations associated with Palbociclib or Telaglenestat. This is complemented by testing the capacity of each gene knockdown (KD) to switch from the drug-adapted state to the control state (Valcarcel et al., 2019). The latter is achieved by running the minimization of metabolic adjustment (MOMA) algorithm while constraining the maximum flux through the reactions of a given gene to 50% of the flux value computed in the drug-adapted state (v_i^{res,qM^2TA}). The MOMA algorithm simulates the effect of perturbations by seeking the flux distribution that minimizes the variation in reaction fluxes compared to v^{res} and subject to the constraints of the gene KD (Segre et al., 2002).

To evaluate the potential of each target, a transformation score (TS) (Valcarcel et al., 2019; Yizhak et al., 2013) is computed as follows:

$$TS = \sum_{m \in DE} \left(W_m \cdot \mathrm{sign}\big(\mathrm{Log}(FC_m)\big) \sum_{i \in R_m} |v_i^{res}| - |v_i^{ref}| \right)$$

Where,

TS is the transformation score.

v_i^{res} is the resulting flux distribution after either running qM^{2}TA with no genes KD (wild type), running qM^{2}TA with a gene KD, or running MOMA with gene KD.

A promising gene target would be any gene whose KD impairs the metabolic transformation from the control to the drug-adapted state while partially reversing the drug-adapted state towards the control state (Supplementary Figure 7). This is measured with the difference between the base TS (i.e., computed when running qM^{2}TA in the wild type) and the TS when running qM^{2}TA and MOMA with a gene KD.

$$Dif_g^{qM^2TA} = \left(TS_{qM^2TA}^{base} - TS_{qM^2TA}^{g_{kd}}\right)$$

$$Dif_g^{MOMA} = \left(TS_{qM^2TA}^{base} - TS_{MOMA}^{g_{kd}}\right)$$

Where:

$TS_{qM^2TA}^{base}$ is the TS score when running qM^{2}TA in the wild type (i.e., without gene KD).

$TS_{qM^2TA}^{g_{kd}}$ is the TS score when running qM^{2}TA with gene *g* KD.

$TS_{MOMA}^{g_{kd}}$ is the TS score when simulating the KD of target genes with MOMA starting from v^{res,M^2TA}

Then, the target score (S_g) for each gene is computed as follows:

$$S_g = 1000 \frac{\left|Dif_g^{qM^2TA} \cdot Dif_g^{MOMA}\right|}{\left(TS_{qM^2TA}^{base}\right)^2} \cdot \min\left(sign\left(Dif_g^{qM^2TA}\right), sign\left(Dif_g^{MOMA}\right)\right)$$

Statistical analysis

Statistical analysis was conducted using GraphPad Prism 7 software (GraphPad Software, San Diego, CA, USA). All data are expressed as mean ± standard deviation (SD), unless otherwise indicated. Shapiro-Wilk test was used to assess the normal distribution of experimental data, Levene's test was employed to evaluate the homogeneity of variances, and Dixon's Q-test was applied to identify outliers. Kruskal-Wallis test or one-way analysis of variance (ANOVA) were used for multiple comparisons between groups. Fisher's least significant difference (LSD) test was used to identify the groups that significantly differed from each other. Two-tailed independent sample Student's *t*-tests were used for comparisons between two conditions, and significant differences were indicated with asterisks. Differences were considered to be significant at $p < 0.05$ (*), $p < 0.01$ (**), and $p < 0.001$ (***). When specified, non-significant differences ($p > 0.05$) are shown as n.s. Differences between groups are indicated with

different letters at $p < 0.05$. Groups with the same letter are not significantly different ($p>0.05$). Concerning gene expression analysis, the DESeq2 package for R was used to evaluate the differential expression between conditions using the Wald Test. The resulting p-values were corrected for multiple testing using the Benjamini-Hochberg function built into DESeq2.

Data availability

RNA-Seq data were deposited into the Gene Expression Omnibus database under accession number GSE245085 and are available at the following URL: https://www.ncbi.nlm.nih.gov/geo/query/acc.cgi?acc=GSE245085.

Acknowledgments

We are grateful for assistance from the Experimental Histopathology and High Throughput Screening facilities at the Francis Crick Institute. This work was supported by the Spanish Ministry of Science and Technology (MCIU/AEI/FEDER, UE; SAF2017-89673-R, MCIN/AEI/10.13039/501100011033; PID2020-115051RB-I00 and PID2019-107139RB-C21), the Interdisciplinary Platform-Global Health (Plataforma Temática Interdisciplinar-Salud Global, PTI-SG; SGL2103019), the Networked Researched Center on Liver and Digestive Diseases (Centro de Investigación en Red en Enfermedades Hepáticas y Digestivas, CIBER-EHD; EHD20PI03 and CB17/04/00023), the Catalan Agency for Universities and Research (AGAUR) (2021-SGR-00350 and 2021-SGR-01490), ICREA Foundation (ICREA Academia award granted to M. Cascante) and The Francis Crick Institute, which receives its core funding from Cancer Research UK (FC001223), the UK Medical Research Council (FC001223) and the Wellcome Trust (FC001223).

Author contributions

M.T-C., M.Y., T.M.T, and M.C. conceived and designed the study. M.T-C. led and performed experiments with J.T-C. M.P., C.H., J.P., E.Z., and I.H.P. assisted with experiments. C.F. and J.J.L. carried out bioinformatics analyses. M.T-C., C.F., T.M.T. and M.C. analyzed the data. A. S-B. analyzed histopathology images. S.M. set up the targeted metabolomics method. M.T-C. and C.F. wrote the manuscript. M.T-C., C.F., J.T-C., M.Y., T.M.T, and M.C. reviewed and revised the manuscript. All authors approved the final manuscript. M.T-C., M.Y., T.M.T, and M.C. secured funding and supervised the study.

Declaration of interests

The authors declare no competing interests.

Figure captions

Figure 1. The antiproliferative effects of Palbociclib and Telaglenestat combination are synergistic and time-dependent.

A. Cell proliferation assay. HCT116 cells were treated with increasing concentrations of Palbociclib, Telaglenestat, or their combination for 96 h, and cell quantification was assessed by Hoechst 33342 staining. Results are shown as the percentage of proliferation relative to untreated cells (mean ± SD for n=6).

B. Spheroid formation assay. Left, scan (top) and phase-contrast microscope (60x, bottom) images of HCT116 spheroids grown on anchorage-independent conditions and treated for 10 days with Palbociclib, the glutaminase inhibitors BPTES and Telaglenestat, or their combination. Right, quantification of total spheroid volume. Spheroids were scored by image acquisition, followed by spheroid area and volume quantification with ImageJ. Results are represented as the percentage of total spheroid volume relative to untreated cells (mean ± SD of n=4).

C. Colony-formation assay. Left, images of HCT116 cells cultured in the absence or presence of 2 μM Palbociclib, 5 μM Telaglenestat, or their combination for 10 days. Right, quantification of the total number of colonies scored by image acquisition with ImageJ.

D. Cell cycle distribution in HCT116 cells treated with Palbociclib, Telaglenestat, or their combination for 96 h and determined by flow cytometry.

E. Cell proliferation curves for HCT116 cells treated with Palbociclib, Telaglenestat or their combination for 96 h. Confluence was monitored in an IncuCyte® S3 (Sartorius) live-cell analysis system. Results are shown as mean ± SD with n=6.

F. Representative IncuCyte® S3 live-cell images in phase-contrast of HCT116 cells treated with Palbociclib, Telaglenestat, or their combination at 96 h. Cell confluence was monitored every 3 h. Scale bar = 400 μm.

G. Cell doubling time of HCT116 cells treated with Palbociclib, Telaglenestat, or their combination. Shown values are the mean ± SD of six independent experiments with six replicates each.

H. Effects of Palbociclib, Telaglenestat or their combination on signaling pathways with time. P-mTOR, mTOR, MYC, GLS1, P-AKT, and HIF 1α protein levels were determined by Western blotting of total protein fractions using β-actin as a loading control.

I, J. Comparative extracellular metabolic fluxes for HCT116 cells treated with Palbociclib, Telaglenestat, or their combination for (H) 96 h and (I) 192 h. Glucose and glutamine consumption and lactate and glutamate production rates were obtained after 24 h of incubation with fresh media and normalized to cell number.

Data information: Concentrations used were 2 μM for palbociclib, 5 μM for Telaglenestat and 10 μM for BPTES. Shown values are mean ± SD for n=3 (except otherwise indicated). Significance was determined by one-way ANOVA and two-tailed independent sample Student's t-tests. Statistically significant differences between treated and control

cells are indicated as $P < 0.05$ (*), $P < 0.01$ (**), and $P < 0.001$ (***), while differences between treatments are shown as $P < 0.05$ (#), $P < 0.01$ (##), and $P < 0.001$ (###).

Figure 2. Palbociclib and Telaglenestat combined therapy significantly suppresses tumor growth *in vivo*.

A. Growth curve of HCT116 xenografts. After one week of tumor establishment, NOD-SCID mice were treated daily for 23 days with vehicle (Control), Palbociclib, Telaglenestat, or their combination, and tumor volume was measured with a Vernier caliper at the indicated days using the modified ellipsoid volume formula: Tumor volume = (length × width^2) × π/6 (n=12 per group). Data are presented as mean ± SEM.

B. Final volume measured at necropsy (n=12 per group). Data are represented in a box and whiskers plot, with the whiskers representing the minimum and maximum values, all data points shown, and the median indicated.

C. Representative *ex vivo* images of solid tumors from each treatment group excised from NOD-SCID mice on Day 31 after cell implantation. Scale bar = 1 cm.

D. Tumor volume fold change from Day 18 (normalized to volume on Day 15) in HCT116 subcutaneous colorectal cancer xenografts (n=12 per group). Data are shown as mean ± SEM.

E. Tumor volume fold change at Day 31 normalized to volume on Day 15 (n=12 per group). Data are represented in a box and whiskers plot, with the whiskers representing the minimum and maximum values, all data points shown, and the median indicated.

F. Bioluminescence intensity relative to the first measurement time point of photon radiance (Day 8) in luciferase-expressing HCT116 xenografts (n=12 per group). Data are shown as mean ± SEM.

G. Tumor growth inhibition (TGI) rate to compare the anti-tumor efficacy of the treatments from Day 18 (n=12 per group) calculated as TGI = $(1-(V_{(T,t)}/V_{(T,0)})/(V_{(C,t)}/V_{(C,0)}))$ x 100, where time 0 is the first measurement of tumor volume on Day 15. Data are presented as mean ± SEM.

H. Representative histopathology images of human colon carcinoma xenografts generated from HCT116 cells; magnification x200, scale bar = 50 µm. Top, Hematoxylin and Eosin (H & E) staining and mitotic figures quantification (mitotic count) expressed as the number of mitoses per 10 high-power fields (HPF), with HPF = 400x overall magnification. Middle, KI67 immunohistochemical staining and quantification of the percentage of KI67 positive cells. Bottom, CD31 immunohistochemical staining and quantification of the percentage of CD31 positive cells. Shown values are mean ± SD for n=3. Statistically significant differences between conditions are indicated with different letters.

Data information: Concentrations used were 100 mg/kg/day p.o. for Palbociclib, 150 mg/kg/day p.o. for Telaglenestat, and 100 mg/kg/day p.o. Palbociclib + 150 mg/kg/day p.o. Telaglenestat for the combination. Shown values are mean ± SD for n=12 (except

where stated otherwise). Significance was determined by ANOVA and Tukey's multiple comparisons test. Statistically significant differences between conditions are indicated as $P < 0.05$ (*), $P < 0.01$ (**), and $P < 0.001$ (***).

Figure 3. Transcriptomic analysis of Palbociclib, Telaglenestat, and their combination treatments *in vivo*.

A. Gene set enrichment analysis (GSEA) results of Palbociclib and Telaglenestat *in vivo* combined treatment compared to control. RNA-Seq was performed on tumors collected after resection and immediately frozen in liquid nitrogen or isopentane. The false discovery rates *q* values (FDR) are indicated for each gene set. A positive normalized enrichment score (NES) value (bars in red) indicates enrichment in the combination treatment phenotype, while a negative NES (bars in green) indicates enrichment in the control phenotype.

B, C. Over-representation analysis (ORA) of downregulated (B) or upregulated (C) gene sets in tumors treated with the combination of Palbociclib and Telaglenestat for 23 days (FDR < 0.25). Genes with FDR < 0.05 were used for the analysis.

D. Schematic representation of the changes in gene expression of the central carbon metabolism caused by Palbociclib (left position in the gene label), Telaglenestat (central position), and their combination (right position) *in vivo* treatments.

E, F. GSEA results of Palbociclib (E) or Telaglenestat (F) *in vivo* treatments compared to control. Gene sets significantly enriched (FDR < 0.25) are ordered by NES. A positive NES value indicates enrichment in the treatment phenotype.

G, H. ORA of downregulated (G) or upregulated (H) gene sets in tumors treated with Telaglenestat for 23 days (FDR < 0.25).

Data information: FDR, False discovery rate; NES, Normalized enrichment score.

Figure 4. Metabolic characterization of *in vivo* tumors

A. Quantification of amino acids in tumors treated with vehicle or the combination of Palbociclib and Telaglenestat using tandem mass spectrometry coupled to liquid chromatography (LC/MS/MS). Significance was determined by a two-tailed independent sample Student's t-tests. Statistically significant differences between treated and control cells are indicated as $P < 0.05$ (*), $P < 0.01$ (**), and $P < 0.001$ (***).

B. Heatmaps of metabolite quantification profiles from tumors treated with vehicle, Palbociclib, Telaglenestat, or the combination of Palbociclib and Telaglenestat obtained by tandem mass spectrometry coupled to liquid chromatography (LC/MS/MS) or flow injection analysis (FIA/MS/MS). For phosphatidylcholines (PC), the total number of carbon atoms and double bonds of the diacyl (aa) or acyl–alkyl (ae) groups is represented by Cx:y, where x indicates the number of carbons and y the number of double bonds. The same notation is used for describing the length and the number of

double bonds in the acyl chain of acylcarnitines (C), lysophosphatidylcholines (lysoPC), sphingomyelins (SM) and hydroxylated sphingomyelins (SM (OH)).

C. Estimation of nitric oxide synthase (NOS), ornithine transcarbamylase (OTC), arginase (ARG), ornithine decarboxylase (ODC), spermidine synthase (SRM), and spermine synthase (SMS) enzyme activities relative to the control condition. Significance was determined by ANOVA and Tukey's multiple comparisons test with α=0.05. Statistically significant differences between conditions are indicated with different letters.

D. Schematic representation of the changes in metabolites, enzyme activities (bold), and gene expression (italics) of the polyamine metabolism and urea cycle caused by Palbociclib and Telaglenestat combined treatment.

E, F. Gene set enrichment analysis (GSEA) results of Palbociclib and Telaglenestat *in vivo* combined treatment compared to palbociclib (E) and Telaglenestat (F) individual treatments. RNA-Seq was performed on tumors collected after resection and immediately frozen in liquid nitrogen or isopentane. The normalized enrichment scores (NES) are indicated for each gene set (FDR *q* value < 0.05). A positive NES value (bars in red) indicates enrichment in the combination treatment phenotype, while a negative NES (bars in green) indicates enrichment in the individual treatment condition.

G. Heatmap of the expression of genes associated with Palbociclib resistance in tumors treated with vehicle, Palbociclib, Telaglenestat, or the combination of Palbociclib and Telaglenestat.

Data information: Ala, alanine; Arg, arginine; Asn, asparagine; Asp, aspartate; Cit, citrulline; Gln, glutamine; Glu, glutamate; Gly, glycine; His, histidine; Ile, isoleucine; Leu, leucine; Lys, lysine; Met, methionine; Orn, ornithine; Phe, phenylalanine; Pro, proline; Ser, serine; Thr, threonine; Trp, tryptophan; Tyr, tyrosine; Val, valine; alpha-AAA, α-aminoadipic acid; Ac-Orn, acetylornithine; Met-SO, methionine sulfoxide; ADMA, asymmetric dimethylarginine; DMA, dimethylarginine; t4-OH-Pro, trans-4-hydroxyproline; SAM, S-adenosylmethionine; AMD, S-adenosylmethionine decarboxylase; dcSAM, decarboxylated SAM; PAOX, polyamine oxidase; SAT1, spermidine/spermine N^1-acetyltransferase; ASS, argininosuccinate synthase; ASL, argininosuccinate lyase. Shown values are mean ± SD for n=4.

Figure 5. Quadratic Multiomic Metabolic Transformation Algorithm (qM^{2}TA).

A. Schematic representation of qM^{2}TA. qM^{2}TA simulates the metabolic flux transition from the control condition to treatment with Palbociclib, Telaglenestat, or Palbociclib and Telaglenestat through the integration of transcriptomics and metabolomics into a genome-scale metabolic model (GSMM). A hypothetic 3D plot of three flux values (v_x,v_y,v_z) and their transition with each treatment is provided.

B. Box plot of log2 fold changes in flux reaction values with each treatment relative to control. Dotted red lines indicate fold changes over 1.25 and under 0.75.

C. Variations in pathways of central carbon and oxidative metabolism with each treatment. Results are expressed as log2 fold changes for total pathway flux relative to the control.

Figure 6. Metabolic characterization of cell lines derived from HCT116 xenografts. Twelve cell lines were obtained from HCT116 tumors from mice that had been treated daily with vehicle, Palbociclib, Telaglenestat, or the combination of Palbociclib and Telaglenestat for 23 days (three cell lines per condition). All cell lines were grown in the absence of chemotherapeutics.

A. Comparative extracellular metabolic fluxes. Glucose and glutamine consumption and lactate and glutamate production rates were assessed after 24 h of incubation with fresh media and normalized to cell number.

B. Cell proliferation curves. Results are shown as fold change of cell proliferation relative to the measurement at 24 h (mean ± SD of n=6). Significance was determined by one-way ANOVA and Tukey's multiple comparisons test. Statistically significant differences between cells derived from tumors that had been treated with the combination and cells obtained from control tumors are indicated as $P < 0.05$ (*).

C. Pool of hexoses consumption rate determined by targeted metabolomics after 24 h of incubation with fresh media and normalized to cell number.

D. Amino acid consumption and production rates were measured after 24 h of incubation with fresh media and normalized to cell number. Significance was determined by a two-tailed independent sample Student's t-test. Statistically significant differences between treated and control cells are indicated as $P < 0.05$ (*), $P < 0.01$ (**), and $P < 0.001$ (***).

E. Quantification of extracellular acidification rate (ECAR) for glycolysis, glycolytic capacity, glycolytic reserve, and non-glycolytic acidification. Cells were cultured in the absence of glucose, and sequential injections of glucose and oligomycin were applied. Data are normalized to cell number and represented as the mean of three independent cell lines for each condition ± SD with n=5.

F. Spheroids comparative extracellular metabolic fluxes. Spheroids were grown in non-adherend conditions for each cell line, and glucose and glutamine consumption and lactate and glutamate production rates were assessed after 96 h of incubation with fresh media and normalized to cell number.

G. Quantification of oxygen consumption rates (OCR), following sequential injections of oligomycin (1 μM), CCCP (600 nM), and antimycin A (2 μM) and rotenone (2 μM), for non-mitochondrial oxygen consumption, basal respiration, maximal respiration, non-ATP linked oxygen consumption (proton leak), ATP production-associated respiration, and spare respiratory capacity. Data are normalized to cell number and shown as the mean of three independent cell lines for each condition ± SD with n=5.

H. Western blotting analysis of total protein fractions for the cell lines generated from tumors using β-actin as a loading control. Each lane corresponds to a different cell line.

I. Quantification of the ATP production rate from glycolysis (glycoATP) and mitochondrial oxidative phosphorylation (mitoATP) and their contribution to the total cellular ATP production rate. Data are normalized to cell number and displayed as the mean of three independent cell lines for each condition ± SD with n=5.

J. Energetic map exhibiting the distribution of mitochondrial ATP (mitoATP) production rate vs. glycolytic ATP (glycoATP) production rate. Cells derived from tumors treated with the combination of Palbociclib and Telaglenestat presented the most quiescent metabolism. Values are expressed as the mean of three independent cell lines for each condition ± SD with n=5.

K. IC_{50} values for palbociclib and the combination of Palbociclib and Telaglenestat in cell lines derived from tumors that had been treated with these inhibitors *in vivo*. Bars represent the mean of the IC_{50} values of three independent cell lines for each condition ± SD with n=6.

Data information: Ala, alanine; Arg, arginine; Asn, asparagine; Asp, aspartate; Cit, citrulline; Gln, glutamine; Glu, glutamate; Gly, glycine; His, histidine; Ile, isoleucine; Leu, leucine; Lys, lysine; Met, methionine; Orn, ornithine; Phe, phenylalanine; Pro, proline; Ser, serine; Thr, threonine; Trp, tryptophan; Tyr, tyrosine; Val, valine. Significance was determined by one-way ANOVA and Tukey's multiple comparisons test with $\alpha=0.05$. Statistically significant differences between conditions are represented with different letters. Data are shown as the mean of three independent cell lines for each condition ± SD with n=3 (except otherwise indicated).

References

Avelar, R. A., Ortega, J. G., Tacutu, R., Tyler, E. J., Bennett, D., Binetti, P., Budovsky, A., Chatsirisupachai, K., Johnson, E., Murray, A.*, et al.* (2020). A multidimensional systems biology analysis of cellular senescence in aging and disease. Genome Biol *21*, 91.

Bankhead, P., Loughrey, M. B., Fernandez, J. A., Dombrowski, Y., McArt, D. G., Dunne, P. D., McQuaid, S., Gray, R. T., Murray, L. J., Coleman, H. G.*, et al.* (2017). QuPath: Open source software for digital pathology image analysis. Sci Rep *7*, 16878.

Beaver, J. A., Amiri-Kordestani, L., Charlab, R., Chen, W., Palmby, T., Tilley, A., Fourie Zirkelbach, J., Yu, J., Liu, Q., Zhao, L.*, et al.* (2015). FDA Approval: Palbociclib for the Treatment of Postmenopausal Patients with Estrogen Receptor-Positive, HER2-Negative Metastatic Breast Cancer. Clin Cancer Res *21*, 4760-4766.

Brunk, E., Sahoo, S., Zielinski, D. C., Altunkaya, A., Drager, A., Mih, N., Gatto, F., Nilsson, A., Preciat Gonzalez, G. A., Aurich, M. K.*, et al.* (2018). Recon3D enables a three-dimensional view of gene variation in human metabolism. Nat Biotechnol *36*, 272-281.

Chen, Y., Zhuang, H., Chen, X., Shi, Z., and Wang, X. (2018). Spermidine-induced growth inhibition and apoptosis via autophagic activation in cervical cancer. Oncol Rep *39*, 2845-2854.

Chou, T. C., and Talalay, P. (1984). Quantitative analysis of dose-effect relationships: the combined effects of multiple drugs or enzyme inhibitors. Adv Enzyme Regul *22*, 27-55.

Conroy, L. R., Lorkiewicz, P., He, L., Yin, X., Zhang, X., Rai, S. N., and Clem, B. F. (2020). Palbociclib treatment alters nucleotide biosynthesis and glutamine dependency in A549 cells. Cancer Cell Int *20*, 280.

Cunningham, J. T., Rodgers, J. T., Arlow, D. H., Vazquez, F., Mootha, V. K., and Puigserver, P. (2007). mTOR controls mitochondrial oxidative function through a YY1-PGC-1alpha transcriptional complex. Nature *450*, 736-740.

Davis, R. T., Blake, K., Ma, D., Gabra, M. B. I., Hernandez, G. A., Phung, A. T., Yang, Y., Maurer, D., Lefebvre, A., Alshetaiwi, H.*, et al.* (2020). Transcriptional diversity and bioenergetic shift in human breast cancer metastasis revealed by single-cell RNA sequencing. Nat Cell Biol *22*, 310-320.

Desbats, M. A., Giacomini, I., Prayer-Galetti, T., and Montopoli, M. (2020). Metabolic Plasticity in Chemotherapy Resistance. Front Oncol *10*, 281.

Dhillon, S. (2015). Palbociclib: first global approval. Drugs *75*, 543-551.

Diaz-Moralli, S., Tarrado-Castellarnau, M., Miranda, A., and Cascante, M. (2013). Targeting Cell Cycle Regulation in Cancer Therapy. Pharmacol Ther *138*, 255-271.

Dossus, L., Kouloura, E., Biessy, C., Viallon, V., Siskos, A. P., Dimou, N., Rinaldi, S., Merritt, M. A., Allen, N., Fortner, R.*, et al.* (2021). Prospective analysis of circulating metabolites and endometrial cancer risk. Gynecol Oncol *162*, 475-481.

Ebrahim, A., Lerman, J. A., Palsson, B. O., and Hyduke, D. R. (2013). COBRApy: COnstraints-Based Reconstruction and Analysis for Python. BMC Systems Biology *7*, 74.

El-Botty, R., Morriset, L., Montaudon, E., Tariq, Z., Schnitzler, A., Bacci, M., Lorito, N., Sourd, L., Huguet, L., Dahmani, A.*, et al.* (2023). Oxidative phosphorylation is a metabolic vulnerability of endocrine therapy and palbociclib resistant metastatic breast cancers. Nat Commun *14*, 4221.

Foguet, C., Xu, Y., Ritchie, S. C., Lambert, S. A., Persyn, E., Nath, A. P., Davenport, E. E., Roberts, D. J., Paul, D. S., Di Angelantonio, E.*, et al.* (2022). Genetically personalised organ-specific metabolic models in health and disease. Nat Commun *13*, 7356.

Fry, D. W., Harvey, P. J., Keller, P. R., Elliott, W. L., Meade, M., Trachet, E., Albassam, M., Zheng, X., Leopold, W. R., Pryer, N. K., and Toogood, P. L. (2004). Specific inhibition of cyclin-dependent kinase 4/6 by PD 0332991 and associated antitumor activity in human tumor xenografts. Mol Cancer Ther *3*, 1427-1438.

Gerner, E. W., and Meyskens, F. L., Jr. (2004). Polyamines and cancer: old molecules, new understanding. Nat Rev Cancer *4*, 781-792.

Goel, S., Bergholz, J. S., and Zhao, J. J. (2022). Targeting CDK4 and CDK6 in cancer. Nat Rev Cancer.

Groenland, S. L., Martinez-Chavez, A., van Dongen, M. G. J., Beijnen, J. H., Schinkel, A. H., Huitema, A. D. R., and Steeghs, N. (2020). Clinical Pharmacokinetics and Pharmacodynamics of the Cyclin-Dependent Kinase 4 and 6 Inhibitors Palbociclib, Ribociclib, and Abemaciclib. Clin Pharmacokinet *59*, 1501-1520.

Gross, M. I., Demo, S. D., Dennison, J. B., Chen, L., Chernov-Rogan, T., Goyal, B., Janes, J. R., Laidig, G. J., Lewis, E. R., Li, J.*, et al.* (2014). Antitumor activity of the glutaminase inhibitor CB-839 in triple-negative breast cancer. Mol Cancer Ther *13*, 890-901.

Gudmundsson, S., and Thiele, I. (2010). Computationally efficient flux variability analysis. BMC Bioinformatics *11*, 489.

Hardie, D. G., Ross, F. A., and Hawley, S. A. (2012). AMPK: a nutrient and energy sensor that maintains energy homeostasis. Nat Rev Mol Cell Biol *13*, 251-262.

Harding, J. J., Telli, M., Munster, P., Voss, M. H., Infante, J. R., DeMichele, A., Dunphy, M., Le, M. H., Molineaux, C., Orford, K.*, et al.* (2021). A Phase I Dose-Escalation and Expansion Study of Telaglenastat in Patients with Advanced or Metastatic Solid Tumors. Clin Cancer Res *27*, 4994-5003.

Heirendt, L., Arreckx, S., Pfau, T., Mendoza, S. N., Richelle, A., Heinken, A., Haraldsdottir, H. S., Wachowiak, J., Keating, S. M., Vlasov, V.*, et al.* (2019). Creation and analysis of biochemical constraint-based models using the COBRA Toolbox v.3.0. Nat Protoc *14*, 639-702.

Hernandez-Segura, A., Nehme, J., and Demaria, M. (2018). Hallmarks of Cellular Senescence. Trends in cell biology *28*, 436-453.

Krug, K., Mertins, P., Zhang, B., Hornbeck, P., Raju, R., Ahmad, R., Szucs, M., Mundt, F., Forestier, D., Jane-Valbuena, J.*, et al.* (2019). A Curated Resource for Phosphosite-specific Signature Analysis. Mol Cell Proteomics *18*, 576-593.

Labrie, M., Brugge, J. S., Mills, G. B., and Zervantonakis, I. K. (2022). Therapy resistance: opportunities created by adaptive responses to targeted therapies in cancer. Nat Rev Cancer.

Li, Q., Dai, W., Liu, J., Li, Y. X., and Li, Y. Y. (2019). DRAP: a toolbox for drug response analysis and visualization tailored for preclinical drug testing on patient-derived xenograft models. J Transl Med *17*, 39.

Liao, Y., Wang, J., Jaehnig, E. J., Shi, Z., and Zhang, B. (2019). WebGestalt 2019: gene set analysis toolkit with revamped UIs and APIs. Nucleic Acids Res *47*, W199-W205.

Liberzon, A., Subramanian, A., Pinchback, R., Thorvaldsdottir, H., Tamayo, P., and Mesirov, J. P. (2011). Molecular signatures database (MSigDB) 3.0. Bioinformatics *27*, 1739-1740.

Litzler, L. C., Zahn, A., Dionne, K. L., Sprumont, A., Ferreira, S. R., Slattery, M. R. F., Methot, S. P., Patenaude, A. M., Hebert, S., Kabir, N.*, et al.* (2023). Protein arginine methyltransferase 1 regulates B cell fate after positive selection in the germinal center in mice. J Exp Med *220*.

Love, M. I., Huber, W., and Anders, S. (2014). Moderated estimation of fold change and dispersion for RNA-seq data with DESeq2. Genome Biol *15*, 550.

Marra, A., and Curigliano, G. (2019). Are all cyclin-dependent kinases 4/6 inhibitors created equal? NPJ Breast Cancer *5*, 27.

McCartney, A., Migliaccio, I., Bonechi, M., Biagioni, C., Romagnoli, D., De Luca, F., Galardi, F., Risi, E., De Santo, I., Benelli, M.*, et al.* (2019). Mechanisms of Resistance to CDK4/6 Inhibitors: Potential Implications and Biomarkers for Clinical Practice. Front Oncol *9*, 666.

Mendez-Lucas, A., Lin, W., Driscoll, P. C., Legrave, N., Novellasdemunt, L., Xie, C., Charles, M., Wilson, Z., Jones, N. P., Rayport, S.*, et al.* (2020). Identifying strategies to target the metabolic flexibility of tumours. Nat Metab *2*, 335-350.

Morita, M., Gravel, S. P., Chenard, V., Sikstrom, K., Zheng, L., Alain, T., Gandin, V., Avizonis, D., Arguello, M., Zakaria, C.*, et al.* (2013). mTORC1 controls mitochondrial activity and biogenesis through 4E-BP-dependent translational regulation. Cell metabolism *18*, 698-711.

Morrish, F., and Hockenbery, D. (2014). MYC and mitochondrial biogenesis. Cold Spring Harb Perspect Med *4*.

O'Leary, B., Finn, R. S., and Turner, N. C. (2016). Treating cancer with selective CDK4/6 inhibitors. Nature reviews Clinical oncology *13*, 417-430.

Pang, Z., Zhou, G., Ewald, J., Chang, L., Hacariz, O., Basu, N., and Xia, J. (2022). Using MetaboAnalyst 5.0 for LC-HRMS spectra processing, multi-omics integration and covariate adjustment of global metabolomics data. Nat Protoc *17*, 1735-1761.

Papadimitriou, M. C., Pazaiti, A., Iliakopoulos, K., Markouli, M., Michalaki, V., and Papadimitriou, C. A. (2022). Resistance to CDK4/6 inhibition: Mechanisms and strategies to overcome a therapeutic problem in the treatment of hormone receptor-positive metastatic breast cancer. Biochim Biophys Acta Mol Cell Res *1869*, 119346.

Pranzini, E., Pardella, E., Paoli, P., Fendt, S. M., and Taddei, M. L. (2021). Metabolic Reprogramming in Anticancer Drug Resistance: A Focus on Amino Acids. Trends Cancer *7*, 682-699.

Qie, S., Yoshida, A., Parnham, S., Oleinik, N., Beeson, G. C., Beeson, C. C., Ogretmen, B., Bass, A. J., Wong, K. K., Rustgi, A. K., and Diehl, J. A. (2019). Targeting glutamine-addiction and overcoming CDK4/6 inhibitor resistance in human esophageal squamous cell carcinoma. Nat Commun *10*, 1296.

Ran, H., Zhu, Y., Deng, R., Zhang, Q., Liu, X., Feng, M., Zhong, J., Lin, S., Tong, X., and Su, Q. (2018). Stearoyl-CoA desaturase-1 promotes colorectal cancer metastasis in response to glucose by suppressing PTEN. J Exp Clin Cancer Res *37*, 54.

Schmidt, B. J., Ebrahim, A., Metz, T. O., Adkins, J. N., Palsson, B. O., and Hyduke, D. R. (2013). GIM3E: condition-specific models of cellular metabolism developed from metabolomics and expression data. Bioinformatics *29*, 2900-2908.

Segre, D., Vitkup, D., and Church, G. M. (2002). Analysis of optimality in natural and perturbed metabolic networks. Proceedings of the National Academy of Sciences of the United States of America *99*, 15112-15117.

Sherr, C. J., Beach, D., and Shapiro, G. I. (2016). Targeting CDK4 and CDK6: From Discovery to Therapy. Cancer Discov *6*, 353-367.

Shukla, K., Ferraris, D. V., Thomas, A. G., Stathis, M., Duvall, B., Delahanty, G., Alt, J., Rais, R., Rojas, C., Gao, P.*, et al.* (2012). Design, synthesis, and pharmacological evaluation of bis-2-(5-phenylacetamido-1,2,4-thiadiazol-2-yl)ethyl sulfide 3 (BPTES) analogs as glutaminase inhibitors. J Med Chem *55*, 10551-10563.

Sica, V., Bravo-San Pedro, J. M., Stoll, G., and Kroemer, G. (2020). Oxidative phosphorylation as a potential therapeutic target for cancer therapy. Int J Cancer *146*, 10-17.

Subramanian, A., Tamayo, P., Mootha, V. K., Mukherjee, S., Ebert, B. L., Gillette, M. A., Paulovich, A., Pomeroy, S. L., Golub, T. R., Lander, E. S., and Mesirov, J. P. (2005). Gene set enrichment analysis: a knowledge-based approach for interpreting genome-wide expression profiles. Proceedings of the National Academy of Sciences of the United States of America *102*, 15545-15550.

Tarrado-Castellarnau, M., Atauri, P. d., and Cascante, M. (2016). Oncogenic regulation of tumor metabolic reprogramming. Oncotarget *7*, 62726-62753.

Tarrado-Castellarnau, M., de Atauri, P., Tarragó-Celada, J., Perarnau, J., Yuneva, M., Thomson, T. M., and Cascante, M. (2017). De novo MYC addiction as an adaptive response of cancer cells to CDK4/6 inhibition. Mol Syst Biol *13*, 940.

Valcarcel, L. V., Torrano, V., Tobalina, L., Carracedo, A., and Planes, F. J. (2019). rMTA: robust metabolic transformation analysis. Bioinformatics *35*, 4350-4355.

Wu, Q., Schapira, M., Arrowsmith, C. H., and Barsyte-Lovejoy, D. (2021). Protein arginine methylation: from enigmatic functions to therapeutic targeting. Nat Rev Drug Discov *20*, 509-530.

Yizhak, K., Gabay, O., Cohen, H., and Ruppin, E. (2013). Model-based identification of drug targets that revert disrupted metabolism and its application to ageing. Nat Commun *4*, 2632.

Zañudo, J. G. T., Barroso-Sousa, R., Jain, E., Jin, Q., Li, T., Buendia-Buendia, J. E., Pereslete, A., Abravanel, D. L., Ferreira, A. R., Wrabel, E.*, et al.* (2022). Genomic and Transcriptomic Determinants of Resistance to CDK4/6 Inhibitors and Response to Combined Exemestane plus Everolimus and Palbociclib in Patients with Metastatic Hormone Receptor Positive Breast Cancer. medRxiv, 2022.2007.2011.22277416.

Zhu, Z., Turner, N. C., Loi, S., Andre, F., Martin, M., Dieras, V., Gelmon, K. A., Harbeck, N., Zhang, C., Cao, J. Q.*, et al.* (2022). Comparative biomarker analysis of PALOMA-2/3 trials for palbociclib. NPJ Precis Oncol *6*, 56.

Figure 1

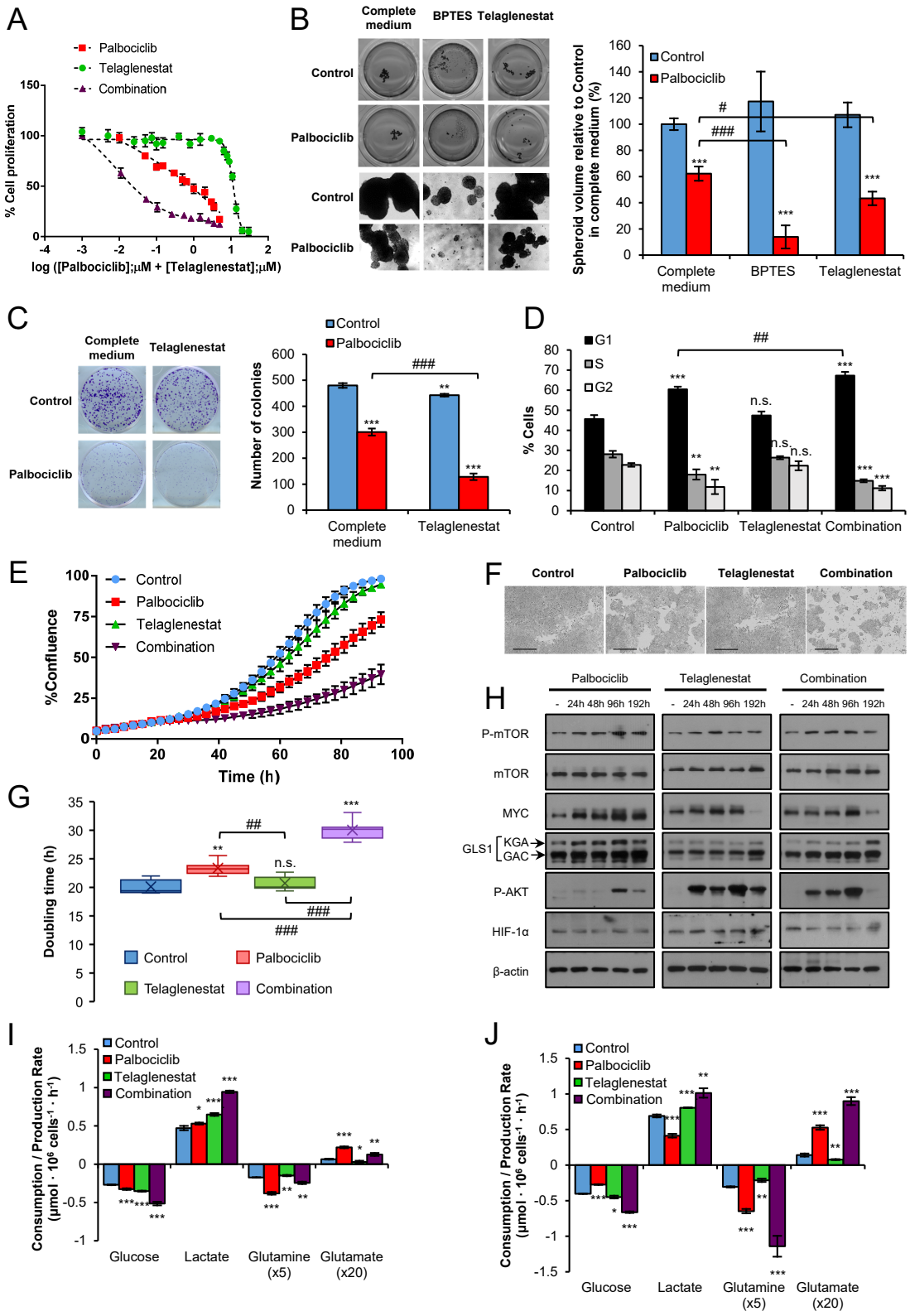
A
Palbociclib
Telaglenestat
Combination
% Cell proliferation
log ([Palbociclib];µM + [Telaglenestat];µM)
B
Complete medium
BPTES
Telaglenestat
Control
Palbociclib
Spheroid volume relative to Control in complete medium (%)
Complete medium
BPTES
Telaglenestat
C
Complete medium
Telaglenestat
Control
Palbociclib
Number of colonies
D
G1
S
G2
% Cells
Control
Palbociclib
Telaglenestat
Combination
E
%Confluence
Time (h)
F
Control
Palbociclib
Telaglenestat
Combination
G
Doubling time (h)
H
P-mTOR
mTOR
MYC
GLS1
KGA
GAC
P-AKT
HIF-1α
β-actin
24h 48h 96h 192h
I
Consumption / Production Rate (µmol · 10⁶ cells⁻¹ · h⁻¹)
Glucose
Lactate
Glutamine (x5)
Glutamate (x20)
J

Figure 2

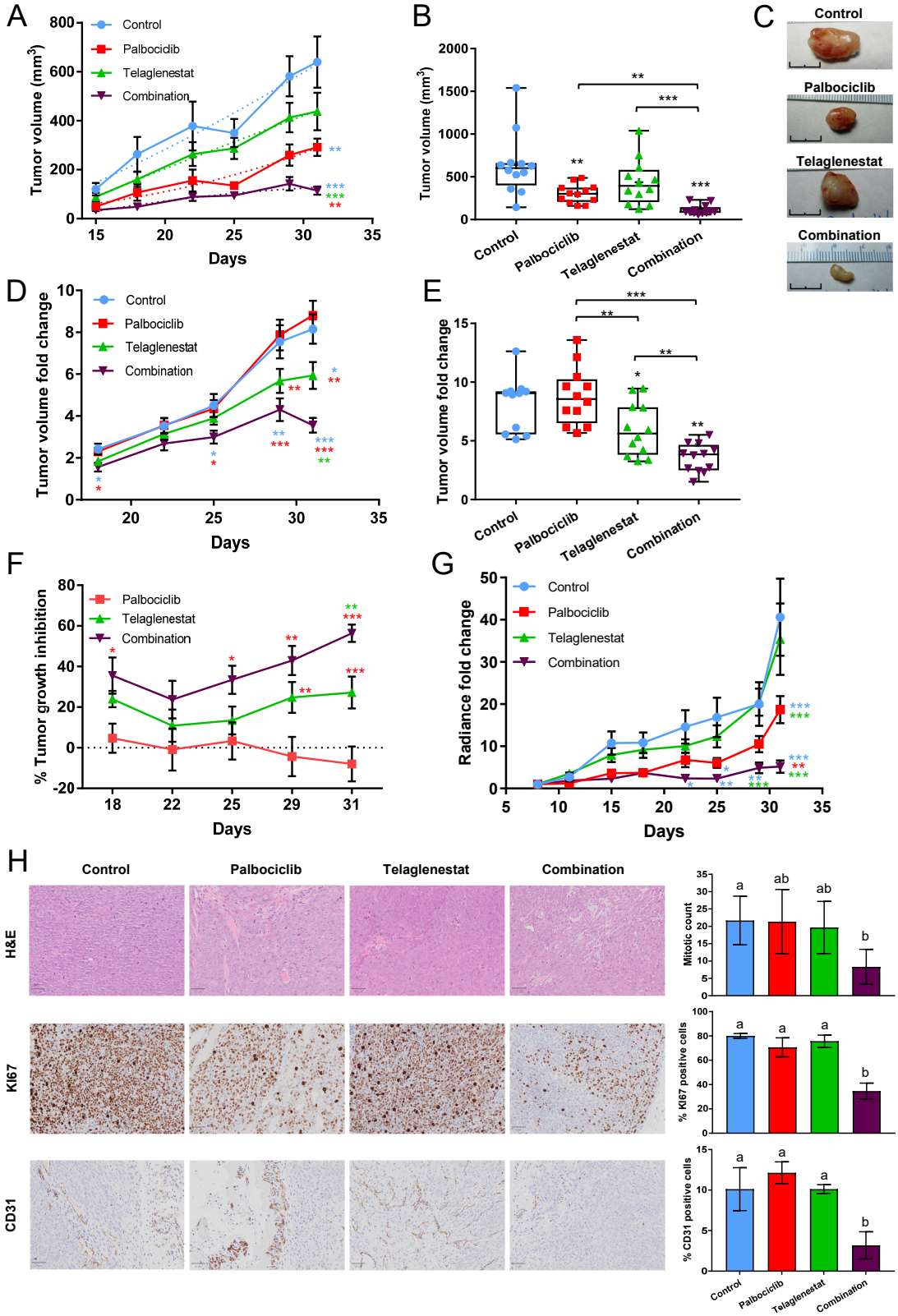
A
Tumor volume (mm3)
Days
Control
Palbociclib
Telaglenestat
Combination
B
Tumor volume (mm3)
Control
Palbociclib
Telaglenestat
Combination
C
Control
Palbociclib
Telaglenestat
Combination
D
Tumor volume fold change
Days
E
Tumor volume fold change
F
% Tumor growth inhibition
Days
G
Radiance fold change
Days
H
Control
Palbociclib
Telaglenestat
Combination
H&E
KI67
CD31
Mitotic count
% KI67 positive cells
% CD31 positive cells

Figure 3

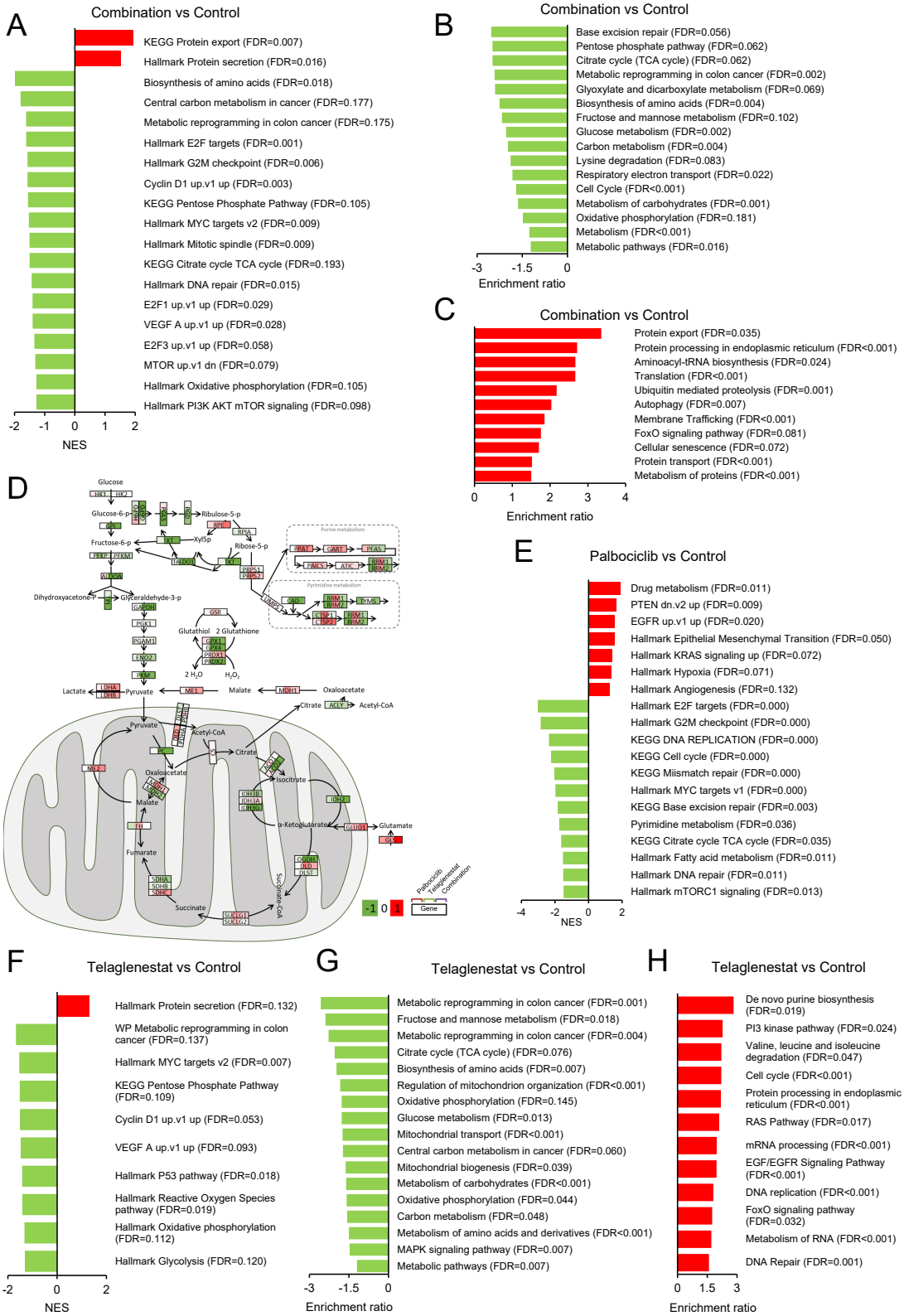
A
Combination vs Control
KEGG Protein export (FDR=0.007)
Hallmark Protein secretion (FDR=0.016)
Biosynthesis of amino acids (FDR=0.018)
Central carbon metabolism in cancer (FDR=0.177)
Metabolic reprogramming in colon cancer (FDR=0.175)
Hallmark E2F targets (FDR=0.001)
Hallmark G2M checkpoint (FDR=0.006)
Cyclin D1 up.v1 up (FDR=0.003)
KEGG Pentose Phosphate Pathway (FDR=0.105)
Hallmark MYC targets v2 (FDR=0.009)
Hallmark Mitotic spindle (FDR=0.009)
KEGG Citrate cycle TCA cycle (FDR=0.193)
Hallmark DNA repair (FDR=0.015)
E2F1 up.v1 up (FDR=0.029)
VEGF A up.v1 up (FDR=0.028)
E2F3 up.v1 up (FDR=0.058)
MTOR up.v1 dn (FDR=0.079)
Hallmark Oxidative phosphorylation (FDR=0.105)
Hallmark PI3K AKT mTOR signaling (FDR=0.098)
-2 -1 0 1 2
NES
B
Combination vs Control
Base excision repair (FDR=0.056)
Pentose phosphate pathway (FDR=0.062)
Citrate cycle (TCA cycle) (FDR=0.062)
Metabolic reprogramming in colon cancer (FDR=0.002)
Glyoxylate and dicarboxylate metabolism (FDR=0.069)
Biosynthesis of amino acids (FDR=0.004)
Fructose and mannose metabolism (FDR=0.102)
Glucose metabolism (FDR=0.002)
Carbon metabolism (FDR=0.004)
Lysine degradation (FDR=0.083)
Respiratory electron transport (FDR=0.022)
Cell Cycle (FDR<0.001)
Metabolism of carbohydrates (FDR=0.001)
Oxidative phosphorylation (FDR=0.181)
Metabolism (FDR<0.001)
Metabolic pathways (FDR=0.016)
-3 -1.5 0
Enrichment ratio
C
Combination vs Control
Protein export (FDR=0.035)
Protein processing in endoplasmic reticulum (FDR<0.001)
Aminoacyl-tRNA biosynthesis (FDR=0.024)
Translation (FDR<0.001)
Ubiquitin mediated proteolysis (FDR=0.001)
Autophagy (FDR=0.007)
Membrane Trafficking (FDR<0.001)
FoxO signaling pathway (FDR=0.081)
Cellular senescence (FDR=0.072)
Protein transport (FDR<0.001)
Metabolism of proteins (FDR<0.001)
0 1 2 3 4
Enrichment ratio
D
Glucose
Glucose-6-p
Fructose-6-p
Ribulose-5-p
Ribose-5-p
Xylu5p
Dihydroxyacetone-P
Glyceraldehyde-3-p
Glutathiol
2 Glutathione
Lactate
Pyruvate
Malate
Oxaloacetate
Citrate
Acetyl-CoA
Isocitrate
α-Ketoglutarate
Glutamate
Fumarate
Succinate
Succinate-CoA
Palbociclib
Telaglenestat
Combination
-1 0 1
Gene
E
Palbociclib vs Control
Drug metabolism (FDR=0.011)
PTEN dn.v2 up (FDR=0.009)
EGFR up.v1 up (FDR=0.020)
Hallmark Epithelial Mesenchymal Transition (FDR=0.050)
Hallmark KRAS signaling up (FDR=0.072)
Hallmark Hypoxia (FDR=0.071)
Hallmark Angiogenesis (FDR=0.132)
Hallmark E2F targets (FDR=0.000)
Hallmark G2M checkpoint (FDR=0.000)
KEGG DNA REPLICATION (FDR=0.000)
KEGG Cell cycle (FDR=0.000)
KEGG Miismatch repair (FDR=0.000)
Hallmark MYC targets v1 (FDR=0.000)
KEGG Base excision repair (FDR=0.003)
Pyrimidine metabolism (FDR=0.036)
KEGG Citrate cycle TCA cycle (FDR=0.035)
Hallmark Fatty acid metabolism (FDR=0.011)
Hallmark DNA repair (FDR=0.011)
Hallmark mTORC1 signaling (FDR=0.013)
-4 -2 0 2
NES
F
Telaglenestat vs Control
Hallmark Protein secretion (FDR=0.132)
WP Metabolic reprogramming in colon cancer (FDR=0.137)
Hallmark MYC targets v2 (FDR=0.007)
KEGG Pentose Phosphate Pathway (FDR=0.109)
Cyclin D1 up.v1 up (FDR=0.053)
VEGF A up.v1 up (FDR=0.093)
Hallmark P53 pathway (FDR=0.018)
Hallmark Reactive Oxygen Species pathway (FDR=0.019)
Hallmark Oxidative phosphorylation (FDR=0.112)
Hallmark Glycolysis (FDR=0.120)
-2 0 2
NES
G
Telaglenestat vs Control
Metabolic reprogramming in colon cancer (FDR=0.001)
Fructose and mannose metabolism (FDR=0.018)
Metabolic reprogramming in colon cancer (FDR=0.004)
Citrate cycle (TCA cycle) (FDR=0.076)
Biosynthesis of amino acids (FDR=0.007)
Regulation of mitochondrion organization (FDR<0.001)
Oxidative phosphorylation (FDR=0.145)
Glucose metabolism (FDR=0.013)
Mitochondrial transport (FDR<0.001)
Central carbon metabolism in cancer (FDR=0.060)
Mitochondrial biogenesis (FDR=0.039)
Metabolism of carbohydrates (FDR<0.001)
Oxidative phosphorylation (FDR=0.044)
Carbon metabolism (FDR=0.048)
Metabolism of amino acids and derivatives (FDR<0.001)
MAPK signaling pathway (FDR=0.007)
Metabolic pathways (FDR=0.007)
-3 -1.5 0
Enrichment ratio
H
Telaglenestat vs Control
De novo purine biosynthesis (FDR=0.019)
PI3 kinase pathway (FDR=0.024)
Valine, leucine and isoleucine degradation (FDR=0.047)
Cell cycle (FDR<0.001)
Protein processing in endoplasmic reticulum (FDR<0.001)
RAS Pathway (FDR=0.017)
mRNA processing (FDR<0.001)
EGF/EGFR Signaling Pathway (FDR<0.001)
DNA replication (FDR<0.001)
FoxO signaling pathway (FDR=0.032)
Metabolism of RNA (FDR<0.001)
DNA Repair (FDR=0.001)
0 1.5 3
Enrichment ratio

Figure 4

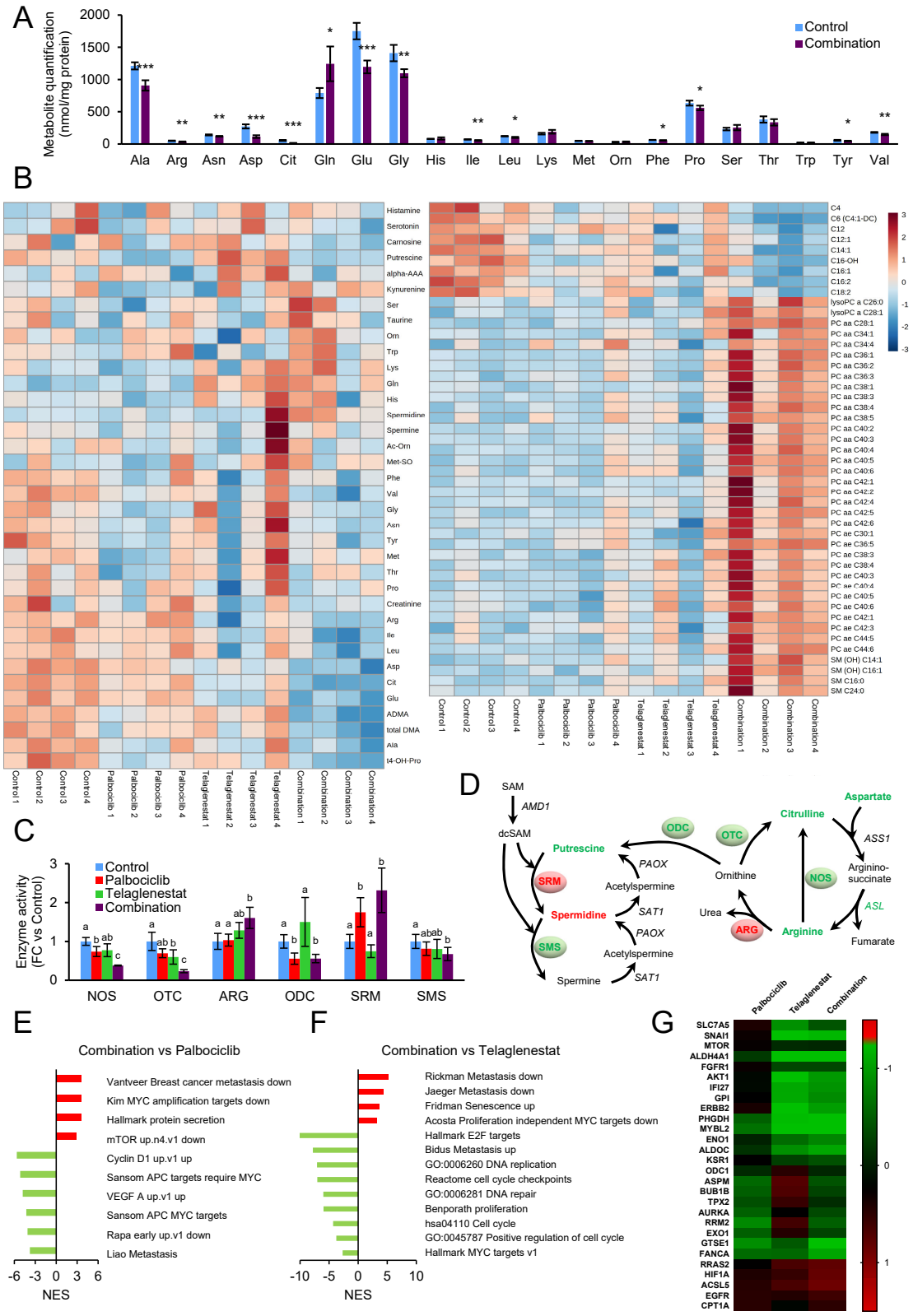
A
Metabolite quantification (nmol/mg protein)
Control
Combination
Ala Arg Asn Asp Cit Gln Glu Gly His Ile Leu Lys Met Orn Phe Pro Ser Thr Trp Tyr Val
B
C
Enzyme activity (FC vs Control)
Control
Palbociclib
Telaglenestat
Combination
NOS OTC ARG ODC SRM SMS
D
SAM
AMD1
dcSAM
Putrescine
SRM
Spermidine
SMS
Spermine
ODC
OTC
PAOX
Acetylspermine
SAT1
Ornithine
Urea
ARG
Citrulline
Aspartate
ASS1
Arginino-succinate
NOS
ASL
Arginine
Fumarate
E
Combination vs Palbociclib
Vantveer Breast cancer metastasis down
Kim MYC amplification targets down
Hallmark protein secretion
mTOR up.n4.v1 down
Cyclin D1 up.v1 up
Sansom APC targets require MYC
VEGF A up.v1 up
Sansom APC MYC targets
Rapa early up.v1 down
Liao Metastasis
NES
F
Combination vs Telaglenestat
Rickman Metastasis down
Jaeger Metastasis down
Fridman Senescence up
Acosta Proliferation independent MYC targets down
Hallmark E2F targets
Bidus Metastasis up
GO:0006260 DNA replication
Reactome cell cycle checkpoints
GO:0006281 DNA repair
Benporath proliferation
hsa04110 Cell cycle
GO:0045787 Positive regulation of cell cycle
Hallmark MYC targets v1
NES
G
Palbociclib
Telaglenestat
Combination
SLC7A5
SNAI1
MTOR
ALDH4A1
FGFR1
AKT1
IFI27
GPI
ERBB2
PHGDH
MYBL2
ENO1
ALDOC
KSR1
ODC1
ASPM
BUB1B
TPX2
AURKA
RRM2
EXO1
GTSE1
FANCA
RRAS2
HIF1A
ACSL5
EGFR
CPT1A

Figure 5

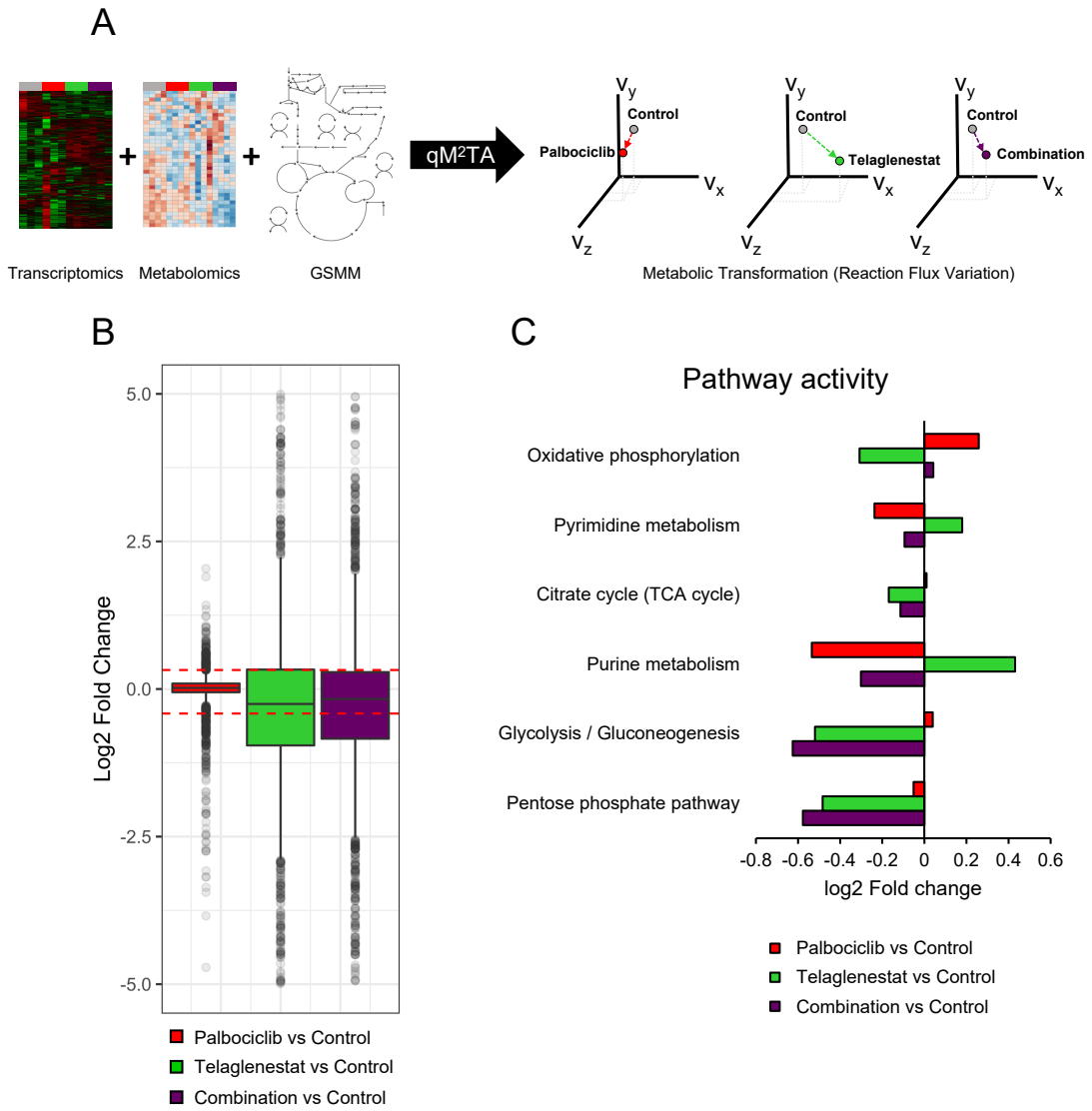
A
Transcriptomics
Metabolomics
GSMM
qM²TA
Control
Palbociclib
Telaglenestat
Combination
Metabolic Transformation (Reaction Flux Variation)
B
Log2 Fold Change
5.0
2.5
0.0
-2.5
-5.0
Palbociclib vs Control
Telaglenestat vs Control
Combination vs Control
C
Pathway activity
Oxidative phosphorylation
Pyrimidine metabolism
Citrate cycle (TCA cycle)
Purine metabolism
Glycolysis / Gluconeogenesis
Pentose phosphate pathway
-0.8 -0.6 -0.4 -0.2 0 0.2 0.4 0.6
log2 Fold change
Palbociclib vs Control
Telaglenestat vs Control
Combination vs Control

Figure 6

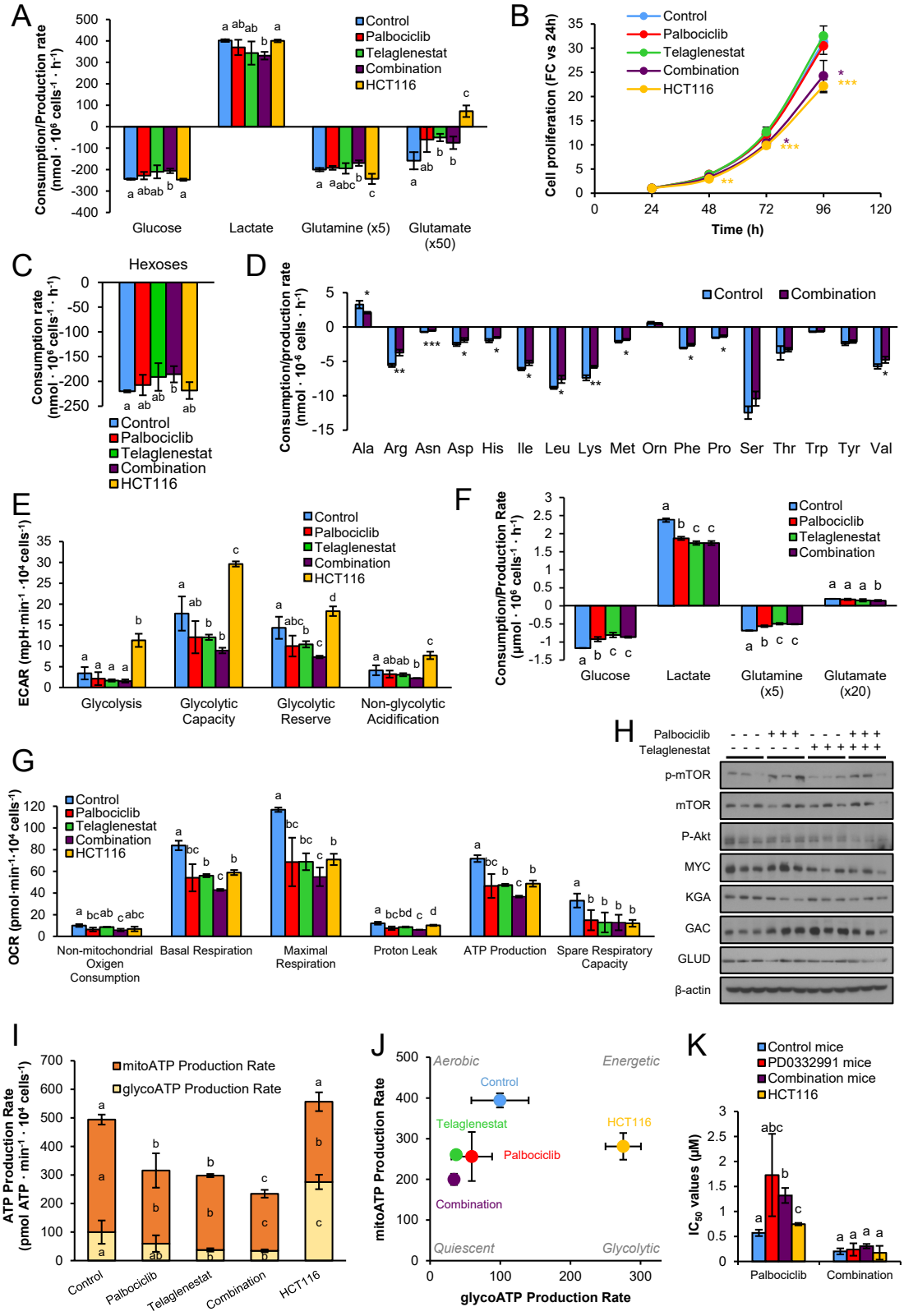
A
Consumption/Production rate (nmol · 10^6 cells^-1 · h^-1)
Control
Palbociclib
Telaglenestat
Combination
HCT116
Glucose
Lactate
Glutamine (x5)
Glutamate (x50)
B
Cell proliferation (FC vs 24h)
Time (h)
C
Hexoses
Consumption rate (nmol · 10^6 cells^-1 · h^-1)
D
Consumption/production rate (nmol · 10^-6 cells · h^-1)
Ala Arg Asn Asp His Ile Leu Lys Met Orn Phe Pro Ser Thr Trp Tyr Val
E
ECAR (mpH·min^-1 · 10^4 cells^-1)
Glycolysis
Glycolytic Capacity
Glycolytic Reserve
Non-glycolytic Acidification
F
Consumption/Production Rate (µmol · 10^6 cells^-1 · h^-1)
Glutamine (x5)
Glutamate (x20)
G
OCR (pmol·min^-1·10^4 cells^-1)
Non-mitochondrial Oxigen Consumption
Basal Respiration
Maximal Respiration
Proton Leak
ATP Production
Spare Respiratory Capacity
H
Palbociclib
Telaglenestat
p-mTOR
mTOR
P-Akt
MYC
KGA
GAC
GLUD
β-actin
I
ATP Production Rate (pmol ATP · min^-1 · 10^4 cells^-1)
mitoATP Production Rate
glycoATP Production Rate
J
mitoATP Production Rate
glycoATP Production Rate
Aerobic
Energetic
Quiescent
Glycolytic
K
Control mice
PD0332991 mice
Combination mice
HCT116
IC50 values (µM)
Palbociclib
Combination